2005

Blind Multiridge Detection and Reconstruction Using Ultrasonic Signals

Rekha Katragadda
Louisiana State University and Agricultural and Mechanical College

BLIND MULTIRIDGE DETECTION AND RECONSTRUCTION USING ULTRASONIC SIGNALS

A Thesis

Submitted to the Graduate Faculty of the
Louisiana State University and
Agricultural and Mechanical College
requirements for the degree of
Master of Science in Electrical Engineering

In

The Department of Electrical & Computer Engineering

by
Rekha Katragadda,
B. Tech, JNTU, India, 2002.
May 2005

Acknowledgments

I am very grateful to my advisor Dr. Hsiao-Chun Wu for his guidance, patience and understanding throughout this work. His suggestions, discussions and constant encouragement have helped me to get a deep insight in the field of Multiridge Detection. I thank Dr. Jerry L. Trahan and Dr. Subhash C. Kak for sparing their time to be a part of my thesis advisory committee. I would also like to specially thank Phani Kiran Mylavarapu of Mechanical Engineering department for his help to understand the ultrasonic nondestructive testing and for providing me with access to their material samples and data, without which this project would not have happened. I would also like to thank all my friends here who made my stay at LSU an enjoyable and a memorable one. Finally, this thesis is dedicated to my parents Bhaskara Rao and Padmavathi and to my sister Radhika.

Table of Contents

List of Tables

List of Figures

Abstract

Time-frequency signal analysis has been widely applied in the modern radar, acoustic, sonar and ultrasonic signal processing techniques. Recently, the nondestructive testing (NDT) techniques via the ultrasonic instrumentation have shown the striking capability of the quality control for the material fabrication industry. In this thesis, we first provide a general mathematical model for the ultrasonic signals collected by pulse-echo sensors and then design a totally blind, novel, signal processing NDT technique relying on neither *a priori* signal information nor any manual effort. The signature signal can be blindly extracted by using the automatic optimal frame size selection for further modeling and characterization of the ultrasonic signal using Gabor analysis. This modeled signature signal is used for multiridge detection and for reconstruction of the signal. The detected ridge information can be used to estimate the transmission and attenuation coefficients, shear modulus, and Young's modulus associated with any arbitrary material sample for fabrication quality control. Thus, our algorithm can be applied for ultrasonic signal characterization and ridge detection in non-destructive testing for new material fabrication. Experimental results show that the ridge detection performance by our proposed method is superior to that of the existing techniques.

Chapter 1: Introduction

1.1 Multiridge Detection and Its Applications

The crucial work in signal processing is to extract useful information or essential features from the given data samples, in order to achieve a better understanding of the underlying physical phenomena, which these data samples are related to. The energy distribution of a wide class of signals at a particular time is concentrated at more than one frequency. Thus, to analyze and classify such energy-compacted (time-frequency localized) signals, the relevant information of the signals has to be attained by extracting the major frequency components within the compacted energy packets [1].

Ridge is defined as a long elevated/raised strip or a long narrow range of hills [2]. Ridges are used to characterize an image (two-dimensional) or a signal (one-dimensional) as the most part of the energy is concentrated in them. A grayscale image may be treated as a height map and the ridges in the map correspond to the drainage lines in its inverted counterpart. Ridge detection is used in many bio-medical applications such as automatic vessel detection from angiogram images [3]. In image processing applications, the ridges are used for global structure extraction, while in one-dimensional (1-D) signals, such as ultrasonic waves in nondestructive testing (NDT), the ridges are related to the cracks or defects in the materials.

The *instantaneous frequency* (IF) can also be estimated from the ridges. IF is used in many applications. For instance, IF can be used in radar signal processing, and it plays a key role in the detection, tracking, and imaging of targets whose radial velocities vary over time, as military targets might if they were making evasive maneuvers [4]. On the

other hand, biomedicine as in the study of electroencephalogram (EEG) signals also benefits from IF estimation techniques. Other applications of instantaneous frequency estimation can also be found in underwater acoustics, oceanography, and seismology [4]. In this thesis, we study one-dimensional (1-D) ultrasonic signals to obtain the important features associated with test materials. In this chapter, introduction to time-frequency analysis and various multiridge detection techniques based on wavelets and Gabor transform is provided. In addition, the problems in the current multiridge detection techniques and the motivation of our work to remove the current limitation on the time-frequency analysis for the ultrasonic signals will be presented.

1.2 Time-Frequency Analysis for Ultrasonic Signals

Time-frequency analysis is a modern branch of harmonic analysis. It comprises all those parts of mathematics and its applications that use the structure of translations and modulations (or time-frequency shifts) for the analysis of functions and operators. Time-frequency analysis is a form of local Fourier analysis that treats time and frequency simultaneously and symmetrically [5].

Since its introduction in the early nineteenth century, the Fourier transform has become the dominant signal analysis tool for many disciplines in science and engineering. Fourier transform is an ideal tool to study stationary signals whose properties are basically time-invariant. Also the frequency contents in the Fourier transform domain can be easily exploited. While the Fourier transform is a very useful means for stationary signals, many signals encountered in real-world situations have time-varying frequency contents. One example is music, where the harmonic (frequency) contents of the acoustic signal change from one note to another. To extract the coherent

features, joint time-frequency transforms have been developed and investigated for characterizing the time-varying frequency content, or the *identity*, of a signal.

The importance of the time-frequency representation can be easily understood by the following example. Consider a short segment of music. If we represent this piece of music as a function of time, we may be able to perceive the transition from one note to the next, but we would have little insight about which notes are in play. On the other hand, the conventional Fourier representation may help us understand the prevailing notes in terms of the frequencies, but the information about the moment of emission and duration associated with the individual notes is not attainable by that means. Although both representations are mathematically correct, neither of them is very satisfactory to reveal the complete characteristics of the signals. According to our physiology, we would prefer a representation that is localized in both time and frequency, like music notation, which tells the musician which note to play at a given moment. Additionally, such a localized time-frequency representation should be discrete, so that it can be easily adapted to different applications.

The best-known time-frequency representation for time series dates back to Gabor and has been referred as the *Short-Time Fourier Transform* (STFT). It is basically a sliding-window Fourier transform [6]. By visualizing the frequency contents of a subject signal as the time-window proceeds, a two-dimensional *time-frequency distribution*, or the so-called *spectrogram*, will be generated. The spectrogram contains information on the snapshots of frequency contents of the signal at different time instants. One well-known drawback of the STFT is that resolution limitation is imposed by the selected window function. The Shorter the window function, the better the time

resolution, but the worse is the frequency resolution, and vice versa [7]. The general concept of wavelet transforms is described in the next section. More detailed theoretical discussions on time-frequency analysis can be found in the two texts by Cohen [8] and Qian and Chen [9].

1.3 Existing Multiridge Detection Techniques

As time-frequency analysis can provide snapshots of time and frequency features, most of the ridge detection algorithms have been utilizing the time-frequency analysis tools. A typical time-frequency analysis tool is the wavelet transform [8]. The wavelet transform is particularly suitable for characterizing transient signals and time varying systems, as they provide compact time-frequency packets [7]. The orthogonal and bi-orthogonal basis functions in the ubiquitous wavelet techniques can lead to fast and reliable algorithms for signal/image transformation, compression and reconstruction. In this section, the mathematical formulation of the wavelet transform will be presented and the associated ridge detection algorithms will be discussed.

1.3.1 Wavelet and Wavelet Families

A wavelet is a zero mean wiggle (no DC frequency component), localized both in time and frequency. For the zero mean condition (also called *admissibility* condition) to be satisfied, it must be oscillatory and hence it is called the wavelet [10]. Given a prototype wavelet $\psi(t)$, its family $\psi_{a,b}(t)$ can be constructed by elementary operations consisting of *time-shifts* and *scaling* (i.e., dilation or contraction). This family of wavelets is defined as:

$$\psi_{a,b}(t) = \frac{1}{a}\psi\left(\frac{t-b}{a}\right),\ b \in R,\ a > 0\,, \tag{1.1}$$

where *a* is the *scaling factor* and *b* is the *time shift*. The prototype wavelet $\psi(t)$ is also called "*mother wavelet*", and it is the intrinsic member of the family corresponding to *b*=0 and *a*=1. The scaling factor *a*>1 corresponds to dilation and *a*<1 to contraction of the mother wavelet.

1.3.2 Continuous Wavelet Transform

The *continuous wavelet transform* of a function $s(t) \in L_2(R)$ is defined as its inner product with a family of admissible wavelets $\psi_{a,b}(t)$, i.e.,

$$T_s(a,b) = < s(t), \psi_{a,b}(t) >_{L_2} = \int_{-\infty}^{\infty} s(t) \psi^*_{a,b}(t) dt \,, \tag{1.2}$$

where *a* and *b* are the scale and time variables respectively, and * denotes complex conjugate. The inverse wavelet transform can also be formulated as [10]:

$$s(t) = \frac{1}{C_\psi} \int_{-\infty}^{\infty} \int_{-\infty}^{\infty} T_s(a,b) \psi_{a,b}(t) \frac{dadb}{a^2}, \tag{1.3}$$

where

$$C_\psi = \int_0^{\infty} \frac{|\Psi(\omega)|^2}{\omega} d\omega \text{ and } \Psi(\omega) = \int_{-\infty}^{\infty} \psi(t) e^{-j\omega t} dt$$

i.e., $\Psi(\omega)$ is the Fourier transform of $\psi(t)$.

In the wavelet transform, the scaling factor *a* will affect both time and frequency contents in the wavelet family as given by Eq. (1.1). The central frequency $\omega_{a,b}$ of the wavelet $\psi_{a,b}(t)$ will be the central frequency $\omega_{1,0}$ of the mother wavelet $\psi(t)$ divided by *a*, such that

$$\omega_{a,b} = \omega_{1,0} / a \,. \tag{1.4}$$

Hence, the effect of the scale *a* is that it stretches the time-domain content (duration) by *a* times but squeezes the frequency-domain content (bandwidth) by *a* times for a wavelet $\psi_{a,b}(t)$.

Therefore, given a mother wavelet $\psi(t)$, the family of wavelets stated in Eq. (1.1) can provide a functional basis for an arbitrary time-frequency localized signal *s*(*t*). The approximation can be achieved by the superimposition of the weighted wavelets such that

$$s(t) \cong \sum_a \sum_b T_s(a,b)\psi_{a,b}(t), \tag{1.5}$$

where $T_s(a,b)$ are the wavelet coefficients.

1.3.3 Ridge Detection Using Continuous Wavelet Transform

As discussed in the previous section, the time-frequency localized signals can be well approximated by the projection onto the wavelet basis functions. Given a proper wavelet basis, we can therefore encode the function *s*(*t*) into the wavelet coefficients $T_s(a,b)$.

The various ridge detection techniques such as Stationary Phase Method (Marseille method) [10], Crazy-Climbers Method [11], Simple Method [10] and SVD method [1] are briefly introduced in this section.

The detection of ridges is based on the following basic principle: the ridge of the wavelet transform $T_S(a,b)$ of the ridge function *s*(*t*) is the set of points (*a, b*) in the transform domain, where the phase of $s(t)\psi^*_{a,b}(t)$ is stationary [6].

1.3.3.1 The Stationary Phase Method

For determining the ridges via the phase of the wavelet coefficients, the stationary phase method can be utilized as follows. Let $\Phi_{(b,a)}$ be the phase of $T_s(b,a)$ defined by Equation (1.6):

$$\Phi_{(b,a)} = \phi_s(t) - \phi_\psi\left(\frac{t-b}{a}\right), \tag{1.6}$$

where ϕ_s and ϕ_ψ are the phase of the signal $s(t)$ and the wavelet $\psi(t)$, respectively.

Differentiation of $\Phi_{(b,a)}$ with respect to scale on the ridge (where $t_0 = b$) gives

$$\left.\frac{\partial \Phi_{(b,a)}}{\partial a}\right|_{a=a_r(b)} = 0 \tag{1.7}$$

Then, for a given time b, the ridge $a_r(b)$ can be found by iteration as the fixed point of Equation (1.7). Similarly, the derivative of $\Phi_{(b,a)}$ with respect to b evaluated on the ridges is

$$\left.\frac{\partial \Phi_{(b,a)}}{\partial b}\right|_{a=a_r(b)} = \frac{1}{a}\phi_\psi'(0), \tag{1.9}$$

and for the Morlet wavelet is

$$\left.\frac{\partial \Phi_{(b,a)}}{\partial b}\right|_{a=a_r(b)} = \frac{\omega_0}{a_r(b)}. \tag{1.10}$$

Again, the ridge $a_r(b)$ can be found by iteration, as the fixed point of Equation (1.10).

The ridge can be extracted from the amplitude or from the phase of $T_s(b,a)$. Theoretically at least, extraction from the phase is more accurate; but not in practice as it involves differentiation of the phase. Thus, extracting the ridge from the modulus of the

signal is more robust than the stationary phase method especially in presence of noise, because the extraction from the modulus does not involve differentiation of the phase.

1.3.3.2 The Crazy-Climbers Method

The method was proposed by Carmona *et al*. and is commonly known as Carmona's method. In this method, multiridge extraction is achieved using the modulus of the continuous wavelet transform. This method is more robust than the other methods mentioned above, as extracting the ridge from the modulus of the transform is more robust than that from the phase and also, the *a priori* information on the ridge can be incorporated in this method as a constraint. The ridge extraction problem can then be transformed into a constrained optimization problem – the constraint being the smoothness of the ridge. Then, this is a direct search procedure that detects all candidate curves $a_r(b)$ that minimize the following penalty function

$$F[a_r(b)] = -\int |T_s(a_r(b),b)|^2 \, db + \int \left[\lambda_1 [a_r'(b)]^2 + \lambda_2 [a_r''(b)]^2\right] db, \qquad (1.11)$$

where the first term maximizes energy density along the ridge and the second term includes the first and second derivatives of the ridge function $a_r(b)$ to assure the smoothness of the ridge. The constants λ_1 and λ_2 can be chosen by the analyst depending on the problem and on how much weight is to be placed on the smoothness constraint.

This optimization problem can be solved by a simulated annealing algorithm which avoids being trapped in local extrema when large-level noise is present.

1.3.3.3 The Simple Method

The most intuitive method for determining the ridges via the continuous wavelet transform, as well as its instantaneous frequency, of a signal is to search the set of (a, b)

which correspond to a local signal peak-amplitude in time [10]. Hence, it is known as the *Simple Method*. This method does not require any *a priori* information or training data regarding the ridges such as its smoothness in Carmona's Method [11], but is more computationally efficient than Carmona's Method which may demand thousands of iterations to converge, and is more stable than the *Marseille Method* [10] because the simple method deals with the amplitudes of the wavelet transform instead of the phases.

Since the moduli of the wavelet transform are peaked along the ridges, then the simplest way of determining the signal ridges is to find the scales at which the scalogram (a local time-frequency energy density is called a scalogram) is locally maximum and satisfies

$$\left.\frac{\partial T_s(a,b;\psi)}{\partial a}\right|_{a=a(b)} = 0 \quad \text{and} \tag{1.13}$$

$$\left.\frac{\partial T_s(a,b;\psi)}{\partial a^2}\right|_{a=a(b)} < 0\,. \tag{1.14}$$

This simple method has good performance in the absence of noise and the resolution for searching (a, b) is small enough.

1.3.3.4 The SVD Method

To further simplify the computational complexity of the aforementioned simple method, an efficient ridge detection algorithm can be achieved using Singular Value Decomposition (SVD) of the scalogram of the mono-component nonstationary and multi-component nonstationary signals in the presence of noise and measurement errors. The main principle involved in this method is based on the following lemma.

Lemma: The Frobenius norm of an MxN matrix A of rank k is

$$E_A = \|A\|^2_F = \sum_{i=1}^{M}\sum_{j=1}^{N} a_{ij}^{\ 2} = \sum_{k=1}^{K} \sigma_k^{\ 2}\ , \tag{1.15}$$

where σ_k are the singular values of A.

According to this lemma, the total energy in the wavelet domain is directly related with the singular values. Since the singular values are in a decreasing order, the dominant energy components are associated with the greater singular values. Hence, the dominant energy concentrations can be easily detected by SVD [4].

1.4 Limitation on the Existing Ridge Detection Algorithms and Motivation of Our Work

A wide class of signals may be conveniently described in terms of time-dependent amplitude and frequency or sums of such amplitude and frequency modulated components. However, the main problem is the numerical estimation of these time-dependent characteristics [11].

To the best of our knowledge, for the extraction of ridges, all the methods use wavelet transforms or equivalent time-frequency representations i.e., all the methods are post-processing of the time-frequency representations. All these methods require *a priori* knowledge and a lot of training data which is difficult to obtain in some cases and is time consuming. Hence, these methods are not practical and optimum for all purposes.

In this thesis, we propose a novel method for the efficient and robust ridge detection of ultrasonic signals. This method does not require any *a priori* knowledge about the signal, instead it blindly detects the ridges.

In this proposed method, no training data is required to extract the *a priori* knowledge. All of the signature signals are extracted dynamically using the given data. This *data-dependent* method blindly extracts the signature signal which is further used

for mutiridge detection. The detected ridges can be used to compute various important parameter values for the materials under consideration. We also mathematically model the ultrasonic signature signal using the Gabor transform and use this as the signal signature to detect the ridges.

Chapter 2. Nondestructive Testing and Signal Processing

2.1. Nondestructive Testing (NDT) and Its Applications

Characterization of material properties is critical for understanding mechanical behavior and design performance of the material under its operating conditions [12, 13]. The necessity to characterize materials for a myriad of applications has spurred the development of many new methods and instruments [14, 15]. However, many mechanical characterization techniques demand destructive sectioning of the material sample to provide desired physical or mechanical measures. On the other hand, *nondestructive testing* (NDT) is defined as a process that produces no alteration of the material being tested [16] i.e., it is free of any intrusion or structural damage of the material samples. NDT is known variously as nondestructive evaluation (NDE), nondestructive characterization, or nondestructive inspection [17]. Most present day sophisticated characterization of materials such as characterization of composites and various mechanical structural troubleshooting can be performed very effectively using NDT. Reliability measurements [18] related to quality assurance can also be performed using NDT. It can also cover almost all other aspects of the general characterization of solids concerning their microstructure, texture, morphology, chemical constituents, physical and chemical properties, as well as the fabrication process.

NDT applications can be adopted not only in industrial and medical fields but also in our daily life. In the industrial area, NDT can be applied in the fabrication of metals, non-metals and all materials containing very small scale to large scale particles. The NDT examinations can be utilized to detect cracks, imperfect welds and junctions, inclusions,

tomography, and surface contamination effects without altering the sample piece in any form. In the medical field, NDT applications include mammography, nuclear magnetic resonance scans, general x-radiography and micro-angiography. Besides, non-contact measurements using sensors are also important to other fields, which range from geology, forensic studies, aerial temperatures and weather surveys, to thickness measurements [17].

One of the most common uses in everyday life for NDT is the authentication of art objects such as paintings, sculptures, furniture, pottery, and ceramics where the tests should be performed without any contact with the object, thus avoiding any friction or smearing damage to the testing surface.

2.2. Various Existing NDT Methods

There are five existing NDT techniques, namely, Radiography, Magnetic Particle Inspection, Liquid Penetrant Inspection, Eddy Current Testing and Ultrasonic Inspection. These methods are briefly introduced in the following sections.

2.2.1 Radiography

Radiography is a technique for obtaining a shadow image of any solid object using penetrating radiation such as x-rays or gamma-rays (γ-rays) [19]. The resulting images recorded in the film are known as *radiographs*. The radiograph obtained is in projection, without any details of the depth of the object. Radiographs are also called as *roentgenograms*, *skiagrams*, *roentgenographs*, or *sciagraphs* [20, 21]. X-radiography is one of the earliest NDT techniques for medical applications.

The contrast in a radiograph is due to the different degrees of absorption of x-rays across the test specimen, and it depends on the variations in specimen thickness, chemical

constituents, densities, flaws or structural discontinuities [19]. During the test, the x-rays are generated and projected through the object to provide high definition and decipherable images. It is required that access to both sides of the test object should be feasible and instrumentation has to operate in a highly-restricted site under stringent safety conditions.

2.2.2. Liquid Penetrant Inspection

Liquid Penetrant Inspection (LPI) is a simple but effective method of examining surface areas for cracks, defects or structural discontinuities [22]. It originated through the observation of blacksmiths that liquids could be seen to seep out of cracks and stain the surface after quenching a hot piece of ironware.

The LPI method is most commonly used, perhaps more than any other method, because of its relative simplicity, low cost and very few limitations on the specimen material or geometry. The LPI equipment is very simple, and the inspection can be performed at many stages in the production of an article as well as after the article has been placed in service.

LPI procedures involve precleaning of the inspection surface, application of the penetrant, observance of a dwell time to allow the penetrant to seep into flaws, removal of excess penetrant, application of a developer again with a dwell time to allow the penetrant to seep out of any surface flaws and to form visible indications. Then, the surface is ready for inspection in a well-lit environment. Finally, the surface may need to be completely cleaned for further use [22]. A permanent record can be made from the liquid penetrant test using photographic methods. The liquid penetrant used in NDT can contain a colored dye, fluorescent dye, visible using UV lamp or a dual sensitivity dye

with both visible coloring and fluorescent components. LPI depends heavily on the visual acuity and ability of the operator. This method is restricted to detect the defects that appear on the surface.

2.2.3. Magnetic Particle Inspection

Magnetic particle inspection (MPI) is a nondestructive testing method used for the defect detection. MPI can be easily manipulated without lengthy procedures and does not require the surface preparation work of the LPI described in the previous section. These advantages make MPI one of the most widely utilized nondestructive testing methods.

In principle, MPI utilizes magnetic fields and small magnetic particles, such as iron filings, to detect flaws in test samples [23]. To achieve satisfactory inspecting ability, the sample being inspected must be made of a ferromagnetic material such as iron, nickel, cobalt, or some of their alloys since the ferromagnetic materials can be magnetized to a sufficient level for effective inspection.

The basic principle involved in MPI is as follows. When a bar magnet is broken at the center of its length, it results into two separate magnets with the magnetic poles on the ends of each piece. If the original magnet is just cracked but not completely dichotomized into two separate pieces, as depicted in Figure 2.1, a north and a south pole will be formed at each edge of the crack. The magnetic field exits from the north pole and enters at the south pole. The magnetic field spreads out when it encounters the small air gap created by the crack because the air cannot support as much magnetic field per unit volume as the magnet can. When the magnetic field spreads out, it appears to leak out of the material and, thus, it is called a *flux leakage field*, as depicted in Figure 2.1 [24].

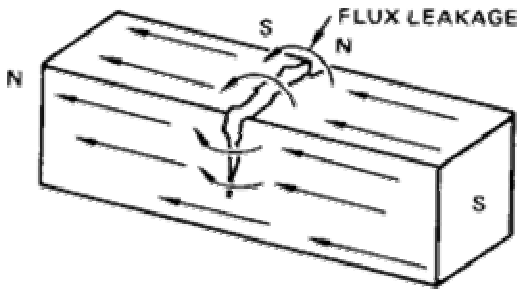

Figure 2.1 The principle of magnetic particle inspection (MPI).

When iron particles are sprinkled on a cracked magnet, they are not only attracted at the ends of the magnet but also at the edges of the crack. This cluster of particles is much easier to observe than the actual crack.

The steps involved in MPI are as follows. The sample surface is first cleaned and is then magnetized to ensure that the magnetic particles are spread over the entire surface, and the excess magnetic particles are removed. It is noted that, in MPI, careful examination and evaluation must be carried out, and additional demagnetization and cleaning work of the specimen is needed after the inspection.

2.2.4. Eddy Current Testing

The basic principle involved in the eddy current testing is as follows. A varying electric current flowing in a coil gives rise to a varying magnetic field. A nearby conductor resists such an effect of the varying magnetic field. This is manifested by an eddy current flowing in a closed loop in the surface layer of the conductor so as to oppose the change and drives a back electromotive force (emf) in the coil. The existence of

cracks and other surface abnormalities modulates the eddy currents generated in the conductor so that the back emf is altered correspondingly [17].

Jean-Bernard Leon Foucault, generally credited with the first clear demonstration of eddy currents, demonstrated that electrical currents are set up in a copper disk moving in a non-uniform magnetic field [17]. Eddy current testing (ET) is plausible when very sensitive electronic devices are available for detecting the subtle changes of the magnetic fields within the sample. Eddy currents are also known as Foucault currents or induced currents, and they can only occur in conducting materials.

2.2.5. Ultrasonic Testing

One typical nondestructive testing is carried out using acoustic waves of high frequency above the audible range, that is, above 20 kHz, which are known as *ultrasound* or *ultrasonics*. Hence, this method of nondestructive testing is called as ultrasonic testing. The frequencies used in the ultrasonic testing range from less than 0.1 MHz to greater than 15 MHz, and typical values of wavelengths in ultrasonic testing are from 1 to 10 mm [25-27].

Ultrasonic testing has been applied in the scientific and engineering world for more than 70 years. Richardson was the first to propose echo-ranging detection of objects in the sea in 1912 following the tragedy of the sinking of the Titanic [17]. Fessenden, in 1914, designed a transducer sensing high-frequency sound waves for submarine signaling and echo-ranging, and it was capable of detecting an iceberg at a range of 2 miles using 1 KHz acoustic waves. In France, Langevin developed a source of ultrasonic waves using the piezoelectric effect, and in 1918, he was able to detect submarines at a distance of 1.5 Km [28]. In 1921, Behun measured the depth of the seabed through an ultrasonic

resonance method using standing waves [29]. In 1929 and 1935, Sokolov proposed the use of ultrasonic waves in detecting defects in metal objects [30], and in 1931, Mulhauser obtained a patent for detecting the flaws in solids using a transmission mode with two transducers. In 1940, Schraiber developed the methods for continuous ultrasonic wave testing. A very important development came from the studies of Firestone in 1940 and Simmons in 1945, namely, *pulsed ultrasonic testing*, using the echo principle [31]. The pulse-echo method [32] in which the same transducer transmits and receives the ultrasonic pulses has become the ubiquitous ultrasonic testing system in recent times.

Ultrasonic analysis for material characterization is based on a simple principle of physics: the motion behavior of any acoustic wave will be influenced by the medium through which it travels. Hence, *structural discontinuities* and *defects* give rise to scattering and reflection of the waves, and the detection of the reflected or transmitted waves is related to the *localization of the defects* [33]. Thus, the changes in one or more of four easily measurable parameters, associated with the passage of a high frequency sound wave through a material, *transit time*, *attenuation*, *scattering*, and *frequency content*, can often be correlated with the changes in physical properties such as *hardness*, *elastic modulus*, *density*, *homogeneity*, or *grain structure* [33]. Thus in this thesis, we try to improve ultrasonic testing techniques by processing ultrasonic signals. The advantages of ultrasonic testing techniques over other existing NDT techniques are provided in Table 2.1.

Table 2.1 Comparison among different nondestructive testing techniques [17]**.**

	Test Method				
	Ultrasonics	**X-ray**	**Eddy Current**	**MPI**	**LPI**
Capital cost	Medium to high	High	Low to medium	Medium	Low
Consumable cost	Very low	High	Low	Medium	Medium
Time of results	Immediate	Delayed	Immediate	Short delay	Short delay
Effect of geometry	Important	Important	Important	Not too important	Not too important
Access problems	Important	Important	Important	Important	Important
Type of defect	Internal	Most	External	External	Surface break
Relative Sensitivity	High	Medium	High	Low	Low
Formal record	Expensive	Standard	Expensive	Unusual	Unusual
Operator skill	High	High	Medium	Low	Low
Operator training	Important	Important	Important	Important	Important
Training needs	High	High	Medium	Low	Low
Portability of equipment	High	Low	High to medium	High to medium	High
Dependent on material composition	Very	Fair	Very	Magnetic only	Little
Ability to automate	Good	Fair	Good	Fair	Fair
Capabilities	Thickness gauging; some composition testing	Thickness gauging	Thickness gauging; grade sorting	Defects only	Defects only

There are two primary methods in ultrasonic nondestructive testing, namely, *transmission* and *reflection* (*pulse-echo) methods*. In the transmission method, testing is performed using two transducers, one for transmitting and the other for receiving, whereas, in the reflection methods, only a single transducer is used for both transmitting and receiving simultaneously. Both these techniques and the corresponding typical ultrasonic responses are illustrated in Figure 2.2 [17].

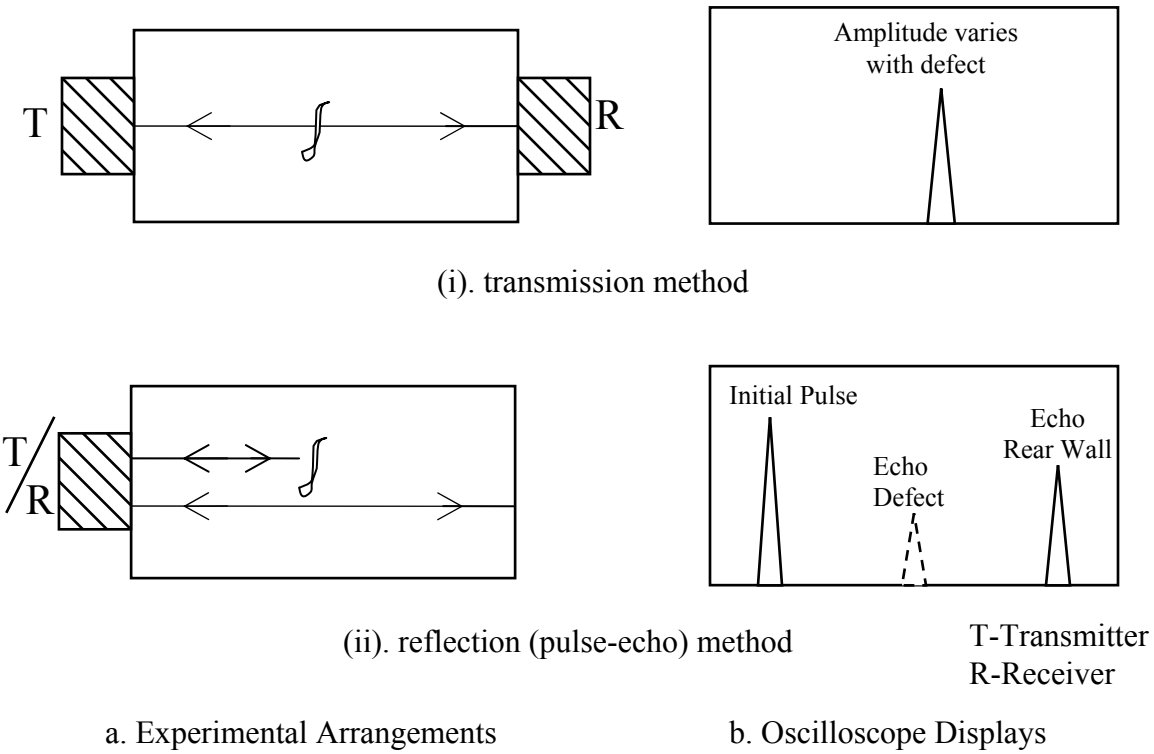

Figure 2.2 Illustration of the ultrasonic testing instruments based on (i) the transmission method and (ii) the reflection (pulse-echo) method.

As illustrated in Figure 2.2, when there is a structural discontinuity or defect, the transducer detects the scattered or reflected wave which can be observed and interpreted as impulses on the oscilloscope by the observer. The only difference between the two techniques is the number of impulses. For the transmission technique, the occurrence of

an impulse will be due to the defect only while for the reflection technique, two additional impulses will always occur due to the top (front-wall) and the bottom (rear-wall) surfaces regardless of any defect.

In the transmission methods, the ultrasonic signal is sent through the specimen (through-transmission) by the transmitting transducer and is collected by the second transducer (receiver) at the other end of the specimen. Thus, the transmission methods require access to both sides of the specimen. The transmission methods, also known as *pulse through-transmission* methods, do not rely on reflected waves and are thus used to detect small defects that do not give adequate reflection in the pulse echo mode, whereas the pulse-echo method (reflection method) can serve for any non-intrusive testing other than defects with weak ultrasonic refection. The pulse through-transmission method is often used for thin metal sheets and for the inspection of composites for large flaws.

In the pulse-echo method, pulses are transmitted and received on the same side of the test panel after being reflected from the objects or the surfaces. In our study, we use the pulse-echo method to collect ultrasonic signals as it is more effective and needs only one transducer. In the pulse-echo method, the single transducer sends a pulse of ultrasonic waves through the specimen which is placed in a coupling liquid, mostly water. The ultrasound travels through the liquid medium and the specimen. The pulses are reflected from the defect (if any present) and also from the rear end of the sample. The reflected ultrasound is sensed by the same transducer. The oscilloscope which can measure both time and amplitude of the transmitted pulse is used to estimate the time required for the pulse to travel the distance between the top and bottom surfaces of the specimen. Usually, a regular train of pulses are sent so that the oscilloscope signal can be

easily observed. The initial pulse may last 1μs (microseconds) and the generation of pulses repeats every millisecond. The presence of a flaw gives rise to a signal reflected earlier than that from the rear surface. This can be visualized from the oscilloscope displays in Figure (2.2). The amplitudes of the reflected signals caused by the defects are attenuated, however, and sometimes the corresponding amplitude levels are very close to the background noise. Therefore, the display on the oscilloscope needs to be interpreted by the observer to determine the location and nature of any flaw in the specimen. Such useful interpretation requires material characterization expertise and full knowledge of the details of the specimen. To remove the aforementioned restriction on the current ultrasonic testing technology, we can adopt the advanced signal processing techniques to provide information like the location, the thickness of the flaw, the velocity of the ultrasonic signal in the specimen, etc. Ultimately, efficient signal processing algorithms can replace any human interpretation effort in ultrasonic testing. Hence, in this thesis we propose a new signal processing technique, multiridge detection, to determine the thickness of the specimen, the velocity of the signal in the specimen, the center frequency and the attenuation of the signal, which are related to other important physical parameters for the materials such as *elastic modulus* and *density*. In the following chapter we will present the mathematical model for ultrasonic signal characterization and introduce our new multiridge detection algorithm.

Chapter 3: Blind Multiridge Detection and Modeling for Ultrasonic Signals

Without loss of generality, in this thesis, we establish the mathematical model for ultrasonic signals using particle-filled composites. The signals are collected giving a sufficient data acquisition window so that all the signal ridges are recorded completely within the acquisition time. Several ridges of various intensities can be found in the received signals and sometimes they are partially overlapped with each other. We will formulate the ridge detection problem and derive a novel algorithm to achieve satisfactory detection performance for the particulate composites. Reliable ridge detection is a very crucial step for automatic mechanical characterization.

Our proposed blind multiridge detection system is depicted in Figure 3.1. It consists of six modules, namely, *ultrasonic signal model*, *energy feature extraction*, *frame-size selection*, *signature signal extraction*, *Gabor parametric modeling* and *correlation detector*. The corresponding mechanisms will be introduced in the following sections.

3.1 Ultrasonic Signal Model

In this section we give a mathematical model for the ultrasonic signals collected by the pulse-echo method. Consider $X(t)$ as the ultrasonic signal collected by the pulse-echo transducer. This continuous-time ultrasonic signal can be formulated as

$$X(t) = \sum_{i=1}^{L} \varpi_i(t) \cos\left(\Omega_0 t + \theta_i\right) + \eta(t), \qquad -\infty < t < \infty, \tag{3.1}$$

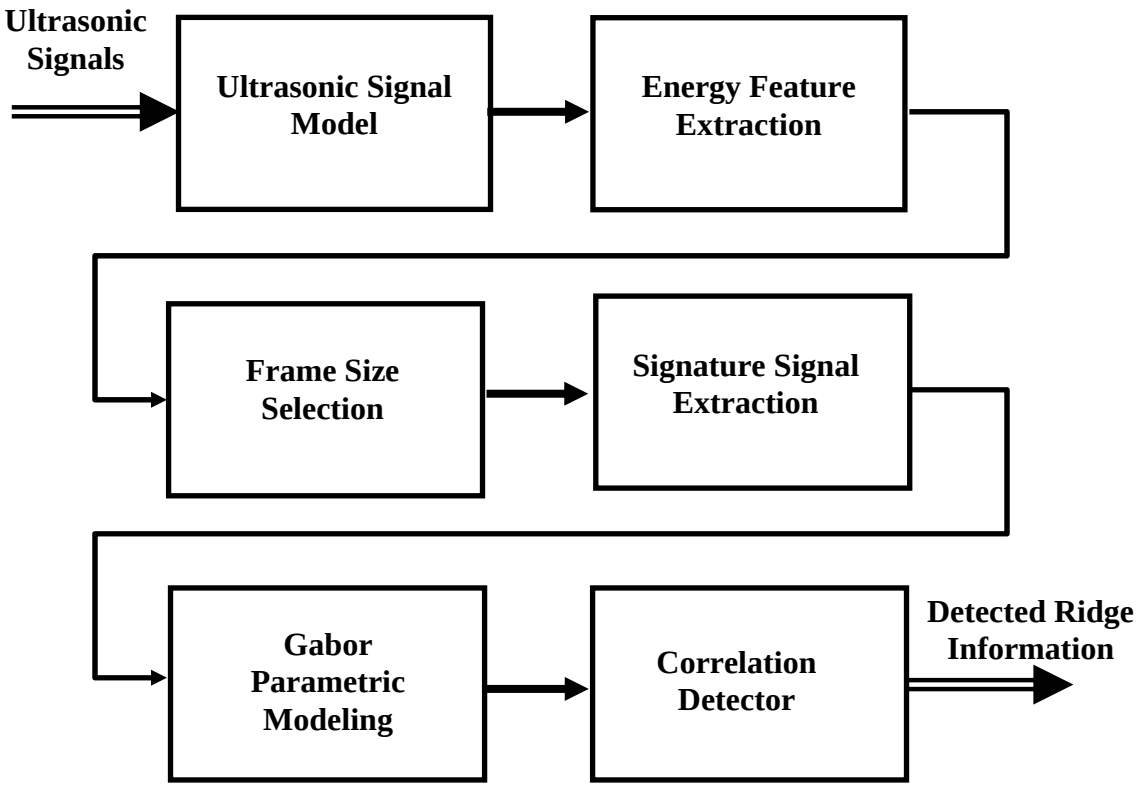

Figure 3.1. Blind Multiridge Detection System.

where $\varpi_i(t)$ is the *envelop waveform* due to the reflection by the interface of two layers ($\varpi_1(t)$ is associated with the top layer and $\varpi_L(t)$ is associated with the bottom layer); Ω_0 is the center frequency of the ultrasonic oscillating signal; θ_i is the phase offset due to the i^{th} interface and $\eta(t)$ is the additive noise. The discrete-time samples of the ultrasonic signal formulated by Eq. (3.1) is written as

$$x(n) = \sum_{i=1}^{L} w_i(n)\cos\left(\omega_0 n + \theta_i\right) + \upsilon(n), \tag{3.2}$$

where $x(n) = X\left(\frac{n}{F_s}\right)$, $\upsilon(n) = \eta\left(\frac{n}{F_s}\right)$, $\omega_0 = \frac{\Omega_0}{F_s}$, $n \in Z$ and F_s is the *sampling frequency*. A typical ultrasonic signal is depicted in Figure (3.2).According to the empirical observation in [34], the discrete-time envelop waveforms $w_i(n)$, $1 \le i \le L$, generally have the following characteristics [41]:

(*i*) $w_i(n)$, $1 \le i \le L$, are the finite-duration window-truncation sequences or *frame functions*, i.e.,

$$w_i(n)\begin{cases} \neq 0, & p_i \le n \le q_i \\ = 0, & otherwise \end{cases}, \; p_i, q_i \in Z \text{ . (finite duration)}$$

(*ii*) $w_i(n)$, $1 \le i \le L$, all have unique peaks, i.e.,

$$w_i(n_{\max,i}) > w_i(n) \ge 0 \text{ , } \forall n \ne n_{\max,i}, \text{ where } p_i < n_{\max,i} < q_i \text{ .}$$

(*iii*) $w_i(n)$, $1 \le i \le L$, all are monotonically increasing functions prior to the occurrence of the peaks, i.e.,

$$w_i(n) > w_i(n-1) \ge 0 \text{ , } n = p_i, p_i + 1, \cdots, n_{\max,i} \text{ .}$$

(*iv*) $w_i(n)$, $1 \le i \le L$, all are monotonically decreasing functions successive to the occurrence of the peaks, i.e.,

$$w_i(n) > w_i(n+1) \ge 0 \text{ , } n = n_{\max,i}, n_{\max,i} + 1, \cdots, q_i - 1, q_i \text{ .}$$

(*v*) The discrete-time Fourier transforms, $W_i(\omega) \equiv \sum_{-\infty}^{\infty} w_i(n) e^{-j\omega n}$, $1 \le i \le L$, all have low-pass narrow-band spectra, i.e.,

$$\frac{\int_{-\omega_{B,i}}^{\omega_{B,i}} |W_i(\omega)|^2 d\omega}{\int_{-\pi}^{\pi} |W_i(\omega)|^2 d\omega} \ge \xi \text{ ,}$$

where ξ is the energy-percentage coefficient assumed to be close to 100% and $\omega_{B,i} << \omega_0$.

(*vi*) The time-average signal autocorrelation functions $r_{ii}(m)$ and signal cross-correlation functions $r_{ii'}(m)$, $1 \le i \le L$, can be defined as

$$r_{ii}(m) \equiv \sum_{n=-\infty}^{\infty} w_i(n) w_i(n+m) \cos(\omega_0 n + \theta_i) \cos(\omega_0 (n+m) + \theta_i)$$

and

$$r_{ii'}(m) \equiv \sum_{n=-\infty}^{\infty} w_i(n) w_{i'}(n+m) \cos(\omega_0 n + \theta_i) \cos(\omega_0 (n+m) + \theta_{i'}).$$

The time-average signal-noise cross-correlation functions can be defined as

$$r_{i\upsilon}(m) \equiv \sum_{n=-\infty}^{\infty} w_i(n) \upsilon(n+m), \; 1 \le i \le L.$$

Then

$$\begin{matrix} \max_m \left[\left| r_{ii}(m) \right| \right] >> \max_m \left[\left| r_{i\upsilon}(m) \right| \right] \\ \max_m \left[\left| r_{ii'}(m) \right| \right] >> \max_m \left[\left| r_{i\upsilon}(m) \right| \right] \end{matrix}, \; \forall i, \forall i'.$$

(*vii*) The time-average signal autocorrelation functions $r_{ii}(m)$ and signal cross-correlation functions $r_{ii'}(m)$, $1 \le i \le L$, both have unique global maxima such that

$$\begin{matrix} \left| r_{ii}(m_{\max}) \right| > \left| r_{ii}(m) \right|, & \forall m \ne m_{\max} \\ \left| r_{ii'}(m'_{\max}) \right| > \left| r_{ii'}(m) \right|, & \forall m \ne m'_{\max} \end{matrix},$$

where

$$\begin{matrix} m_{\max} \equiv \arg\max_m \left(\left| r_{ii}(m) \right| \right) = 0 \\ m'_{\max} \equiv \arg\max_m \left(\left| r_{ii'}(m) \right| \right) \approx n_{\max,i'} - n_{\max,i} \end{matrix}.$$

A typical ultrasonic signal is shown in Figure (3.2) below.

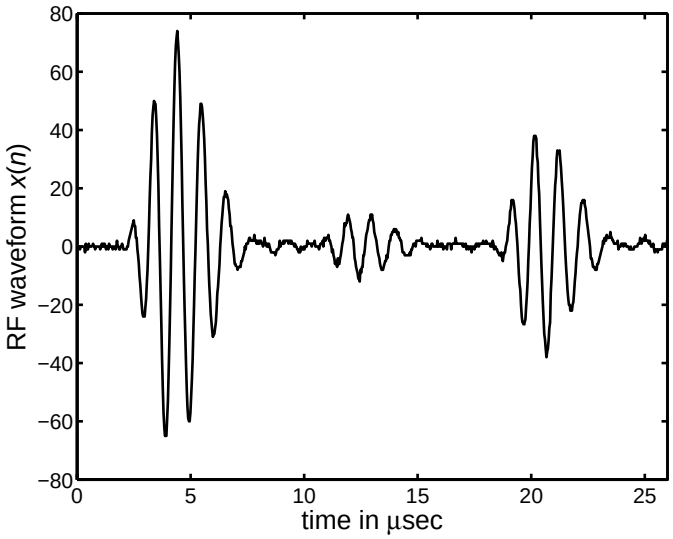

Figure 3.2 A typical Ultrasonic signal

According to the aforementioned characteristics of the ultrasonic signals, it is noted that the ultrasonic signal formulated by Eq. (3.2) can be described as a finite-duration pulse-shaping sinusoid, which is very similar to narrow-band digital communication signals [35]. Once the sinusoidal waveform $\cos(\omega_0 n + \theta_i)$ is given, the pulse function $w_i(n)$ can be extracted by a *frequency down-converter* and a *low-pass filter* [35]. In this ultrasonic signal detection problem, however, all parameters ω_0, θ_i, p_i, q_i, $\omega_{B,i}$, L, associated with $x(n)$ and $w_i(n)$, $1 \le i \le L$, are unknown and therefore the conventional *demodulation* technique cannot be applied [35]. Thus, blind signal processing without any manual operation is considered here for arbitrary material samples. In this paper, the goal is to automatically estimate the number of the interfaces L and detect the *peak locations*: $\arg\max_n \{w_i(n)\cos(\omega_0 n + \theta_i)\}$ and the corresponding *peak values*: $\max_n \{w_i(n)\cos(\omega_0 n + \theta_i)\}$, $1 \le i \le L$.

3.2 Blind Signature Signal Extraction

Since different ultrasonic signals generated by the transducers would vary a lot in their waveforms among different material samples, $w_i(n)\cos(\omega_0 n + \theta_i)$ described in Eq. (3.2) cannot easily be generalized using a specific mathematical function for all types of materials. *A priori* knowledge regarding the optimal frame functions $w_i(n)$ and optimal modulation sinusoids $\cos(\omega_0 n + \theta_i)$ using a large amount of training data has to be presumptive in the existing techniques [11, 37]. However, it would be unrealistic for the ultrasonic NDT for a wide variety of fabricated materials because a lot of expert-driven calibration effort has to be involved once a new material is manufactured. Therefore in this paper, we propose a novel *data-dependent* method to blindly extract the *signal features* for ultrasonic nondestructive testing. According to the mathematical model for ultrasonic signals described in the previous section, the *signature signal* can be defined as the signal segment $\psi(n)$ with the dominant peak, usually the first windowed signal segment in time, i.e.,

$$\psi(n) \equiv w_1(n)\cos(\omega_0 n + \theta_1), \tag{3.3}$$

where $w_1(n_{\max,1}) \geq w_i(n_{\max,i})$, $\forall i \neq 1$.

3.2.1 Energy Features for Signature Signal Extraction

Energy features have been applied for transient signal detection and empirically lead to robust performance in practice [37-39]. We use the *framed energy* here to detect the beginning and the end of the signature signal $\psi(n)$. The framed energy, which depends on the frame size and can be considered as the transformation from the signal sequence, i.e., $x(n),\ n \in Z \xrightarrow{\Gamma_{N_f,\Delta}} E_{N_f,\Delta}(k),\ k \in Z$, is defined as [41]

$$E_{N_f,\Delta}(k) = \Gamma_{N_f,\Delta}[x(n)] \equiv \frac{1}{N_f} \sum_{n=(k-1)\Delta+1}^{(k-1)\Delta+N_f} x^2(n) \tag{3.4}$$

$$= \frac{1}{N_f} \sum_{n=(k-1)\Delta+1}^{(k-1)\Delta+N_f} \sum_{i=1}^{L} \sum_{i'=1}^{L} \frac{1}{2} w_i(n) w_{i'}(n) \left[\cos\left(2\omega_0 n + \theta_i + \theta_{i'}\right) + \cos\left(\theta_i - \theta_{i'}\right)\right]$$

$$+ \frac{1}{N_f} \sum_{n=(k-1)\Delta+1}^{(k-1)\Delta+N_f} \sum_{i=1}^{L} 2w_i(n) \cos\left(\omega_0 n + \theta_i\right) \upsilon(n) + \frac{1}{N_f} \sum_{n=(k-1)\Delta+1}^{(k-1)\Delta+N_f} \upsilon^2(n),$$

where N_f is the *energy-frame size*, Δ is the *frame forwarding size*, k is the *frame index* and $k = 1, 2, \cdots$. If the energy-frame size N_f is carefully chosen, the framed energy sequence $E_{N_f,\Delta}(k)$ would be a smooth function (monotonically-increasing-then-monotonically-decreasing) in the presence of the signature sequence. On the other hand, $E_{N_f,\Delta}(k)$ would be a small constant in the absence of the signature sequence.

In the next two sections, we see why it is important to have the optimal frame-size and then brief the details of the optimal frame selection technique, respectively, for optimal ridge detection.

3.2.2 Frame-size Dilemma

The shape of the energy sequence $E_{N_f,\Delta}(k)$ is rather sensitive to the frame size N_f. Optimal ridge detection can be achieved when $E_{N_f,\Delta}(k)$ has a smooth shape (least spiky) in each individual ridge interval $[p_i, q_i]_{i=1,2,\cdots,L}$. The spikes are associated with the high-frequency components in the Fourier spectrum. Therefore, we investigate the effect of the frame size N_f on the frequency spectrum of $E_{N_f,\Delta}(k)$ at first. The discrete-time Fourier transform of $E_{N_f,\Delta}(k)$ is given by [41]

$$\Xi_{N_f,\Delta}(\omega) \equiv \sum_{k=-\infty}^{\infty} E_{N_f,\Delta}(k) e^{-j\omega k} . \tag{3.5}$$

To simplify our analysis in the absence of $\upsilon(n)$, we assume that the durations of any two different frame functions do not overlap with each other, i.e.,

$$p_i > q_{i-1}, \text{ for } i = 2,3,\cdots,L, \text{ or } w_i(n) w_{i'}(n) = 0, \ \forall i \neq i', \ \forall n .$$

Thus, the framed energy sequence $E_{N_f,\Delta}(k)$ can be reduced as [41]

$$E_{N_f,\Delta}(k) = \frac{1}{N_f} \sum_{i=1}^{L} \sum_{n=-\infty}^{\infty} w_i^2(n) \cos^2(\omega_0 n + \theta_i) rect\left(\frac{n-(k-1)\Delta-1}{N_f} \right), \tag{3.6}$$

$$\text{where } rect\left(\frac{n-(k-1)\Delta-1}{N_f} \right) = \begin{cases} 1, & (k-1)\Delta+1 \le n \le (k-1)\Delta+N_f \\ 0, & elsewhere \end{cases} \quad \text{and } k = 1,2,\cdots .$$

Consequently, according to Eqs. (3.5), (3.6), the Fourier spectrum of $E_{N_f,\Delta}(k)$ can be simplified as [41]

$$\Xi_{N_f,\Delta}(\omega) = \frac{1}{N_f} \sum_{k=-\infty}^{\infty} \sum_{i=1}^{L} \sum_{n=-\infty}^{\infty} w_i^2(n) \cos^2(\omega_0 n + \theta_i) rect\left(\frac{n-(k-1)\Delta-1}{N_f} \right) e^{-j\omega k}$$

$$= \frac{1}{N_f} \sum_{i=1}^{L} \sum_{n=p_i}^{q_i} w_i^2(n) \cos^2(\omega_0 n + \theta_i) \sum_{k=\left\lceil \frac{n-N_f}{\Delta} \right\rceil + 1}^{\left\lfloor \frac{n-1}{\Delta} \right\rfloor + 1} e^{-j\omega k}$$

$$= \frac{1}{N_f} \sum_{i=1}^{L} \sum_{n=p_i}^{q_i} w_i^2(n) \cos^2(\omega_0 n + \theta_i) \Psi_n(\omega), \tag{3.7}$$

where $\lfloor \ \rfloor$ and $\lceil \ \rceil$ are integer rounding down and integer rounding up operators respectively; b is either 0 or 1 dependent on n, Δ and N_f and

$$\Psi_n(\omega) \equiv \frac{\sin\left(\frac{\omega}{2}\left(\left\lfloor \frac{N_f - 1}{\Delta} \right\rfloor + b\right)\right)}{\sin\left(\frac{\omega}{2}\right)} \exp\left(-j\frac{\omega}{2}\left(\left\lfloor \frac{n-1}{\Delta} \right\rfloor + \left\lceil \frac{n - N_f}{\Delta} \right\rceil + 2\right)\right). \tag{3.8}$$

According to [42], the *null-to-null bandwidth* of the frequency spectrum as given by Eq. (3.8) can be calculated as $\frac{4\pi}{\left\lfloor \frac{N_f - 1}{\Delta} \right\rfloor + b}$ radians. The spectral shape of $\Xi_{N_f,\Delta}(\omega)$ is complicated to analyze. However, we can loosely quantify the bandwidth using the upper bound of the magnitude spectrum $\left|\Xi_{N_f,\Delta}(\omega)\right|$. According to Eqs. (3.7) and (3.8), it is obvious that [41]

$$\begin{aligned}\left|\Xi_{N_f,\Delta}(\omega)\right| &\le \frac{1}{N_f}\sum_{i=1}^{L}\sum_{n=p_i}^{q_i} w_i^2(n)\cos^2(\omega_0 n + \theta_i)\left|\Psi_n(\omega)\right| \\ &= \frac{1}{N_f}\sum_{i=1}^{L}\sum_{n=p_i}^{q_i} w_i^2(n)\cos^2(\omega_0 n + \theta_i)\frac{\left|\sin\left(\frac{\omega}{2}\left(\left\lfloor \frac{N_f - 1}{\Delta} \right\rfloor + b\right)\right)\right|}{\left|\sin\left(\frac{\omega}{2}\right)\right|}.\end{aligned} \tag{3.9}$$

Based on the inequality in Eq. (3.9), we can conclude that the magnitude of the sidelobes, namely, $\left|\Xi_{N_f,\Delta}(\omega)\right|$, for $|\omega| \ge \frac{2\pi}{\left\lfloor \frac{N_f - 1}{\Delta} \right\rfloor + b}$, in the frequency domain, can be considered relatively small compared to the DC frequency component $\left|\Xi_{N_f,\Delta}(0)\right|$. In other words, the bandwidth of $\Xi_{N_f,\Delta}(\omega)$ can be roughly defined as $\frac{4\pi}{\left\lfloor \frac{N_f - 1}{\Delta} \right\rfloor + b}$. It turns out to be the fact that the larger N_f, the less high frequency component will appear in the framed

energy sequence $E_{N_f,\Delta}(k)$. However, if N_f is too large, the bandwidth of $\Xi_{N_f,\Delta}(\omega)$ appears to be very narrow and therefore $E_{N_f,\Delta}(k)$ appears to be a constant sequence, which can not provide informative features for a reliable ridge detection.

3.2.3 Optimal Frame-size Selection Technique

The optimal frame-size for a framed-energy sequence $E_{N_f,\Delta}(k)$ can be achieved when it appears to have a both smooth and compact-duration shape. From the discussion in *Section 3.2.2*, it is noted that the smoothness can be achieved once we choose a large frame-size N_f while the compact-duration can be achieved once we choose a small frame-size N_f. We provide here an algorithm to seek the trade-off between these two goals. In our algorithm, we have applied a *nonlinear programming* statement to optimize the frame-size N_f. The goal of achieving a compact-duration $E_{N_f,\Delta}(k)$ becomes a nonlinear constraint. We would like to maximize the frame-size N_f subject to this constraint. Since the goal of a compact duration $E_{N_f,\Delta}(k)$ is to achieve a *fast-increasing-and-then-fast-decreasing* or *steep* waveform and $E_{N_f,\Delta}(k) \geq 0$, we propose to adopt the *kurtosis function* $kur\left(E_{N_f,\Delta}(k)\right)$ [43] to construct a new constraint function. The kurtosis $kur\left(E_{N_f,\Delta}(k)\right)$ for the energy sequence E_k, given a specific frame-size N_f and a frame forwarding size Δ, can be defined as [41]

$$kur\left(E_{N_f,\Delta}(k)\right) \equiv \frac{\sum_k P_k\left[(k-1)\Delta+1-M\right]^4}{\left(\sum_k P_k\left[(k-1)\Delta+1-M\right]^2\right)^2}, \tag{3.10}$$

where P_k is the sequence satisfying the *probability axioms* [43] and it results from $E_{N_f,\Delta}(k)$ such that [41]

$$P_k \equiv \frac{E_{N_f,\Delta}(k)}{\sum_k E_{N_f,\Delta}(k)}, \tag{3.11}$$

and the mean M can be given by

$$M \equiv \sum_k P_k\left[(k-1)\Delta + 1\right]. \tag{3.12}$$

This measure will be insensitive to any arbitrary time delay [41]. It simply means that we can start to collect the signal at any time for the mechanical property characterization. The *optimal frame-size* N_f^* can be achieved according to the following criterion [41]:

$$N_f^* = \arg\max\left(N_f\right)$$

$$\text{subject to} \quad \frac{\left|kur\left(E_{N_f,\Delta}(k)\right) - kur\left(E_{N_f+\delta N,\Delta}(k)\right)\right|}{kur\left(E_{N_f,\Delta}(k)\right)} \le \kappa_{th}\ , \tag{3.13}$$

where $kur\left(E_{N_f,\Delta}(k)\right)$ can be formulated using Eqs. (3.10), (3.11) and (3.12) and κ_{th} is the presumptive upper bound for our proposed *kurtosis sensitivity constraint function* $\frac{\left|kur\left(E_{N_f,\Delta}(k)\right) - kur\left(E_{N_f+\delta N,\Delta}(k)\right)\right|}{kur\left(E_{N_f,\Delta}(k)\right)}$ and δN is the *incremental frame-size*.

3.2.4 Signature Signal Extraction

Once the optimal frame-size is selected according to Eq. (3.13), we can construct the energy sequence E_k using $N_f = N_f^*$. Thus if the $k_p{}^{th}$ frame contains the peak value $w_1(n_{\max,1})$ of the signature signal $\psi(n)$, it can be calculated as $k_p = \arg\max_k\left(E_k\right)$. Then

the duration $[p_1, q_1]$ of the signature signal $\psi(n) = w_1(n)\cos(\omega_0 n + \theta_1)$ can be estimated as [41]

$$\begin{aligned} \hat{p}_1 &= (k_s - 1)\Delta + 1 \\ \hat{q}_1 &= (k_e - 1)\Delta + N_f^* \end{aligned}, \tag{3.14}$$

where k_s, k_e are the first energy frames satisfying $E_{k_s} < \varepsilon_{th}$ and $E_{k_e} < \varepsilon_{th}$ during the count-down and the count-up, respectively, starting from the frame index k_p; ε_{th} is the predetermined *energy threshold*. According to Eq. (3.14), the signature signal can be estimated as

$$\hat{\psi}(n) = \begin{cases} x(n), & \hat{p}_1 \le n \le \hat{q}_1 \\ 0, & elsewhere \end{cases}. \tag{3.15}$$

Thereupon, the *peak location* $\hat{n}_{\max,1}$ in the signature signal can also be estimated as

$$\hat{n}_{\max,1} = \arg\max_n [\hat{\psi}(n)]. \tag{3.16}$$

3.3 Gabor Analysis for Signature Signal Extraction

After extracting the signature signal, we would like to model the ultrasonic signal by applying the Gabor analysis. According to the Gabor analysis, any ultrasonic signal $x(n)$ can be represented as a series of *elementary functions*, which are constructed from the translations and modulations of a single building block $g_i(n)$, such that

$$x(n) \approx \mathrm{Re}\left\{ \sum_i \sum_m c_{i,m} g_{i,m}(n) \right\}, \tag{3.17}$$

where m, i are the time and scale parameters respectively and the elementary functions are given by

$$g_{i,m}(n) \equiv g_i(n-m) e^{j(\omega_0 i n + \theta)}, \forall i, m \in Z^+ . \tag{3.18}$$

The short-time window function $g_i(n)$, also known as the frame function, in Eq (3.18) needs to be determined. Of all window shapes, the Gaussian window leads to the highest time-frequency resolution. Gaussian window function is optimal since it has the smallest time-frequency bandwidth product and it can represent the most localized element signals in the time-frequency packets [44].

A typical set of Gabor elementary functions is illustrated in Figure (3.3) below. The representation of a signal as a series of translation and modulation of the elementary functions can be clearly understood by these figures.

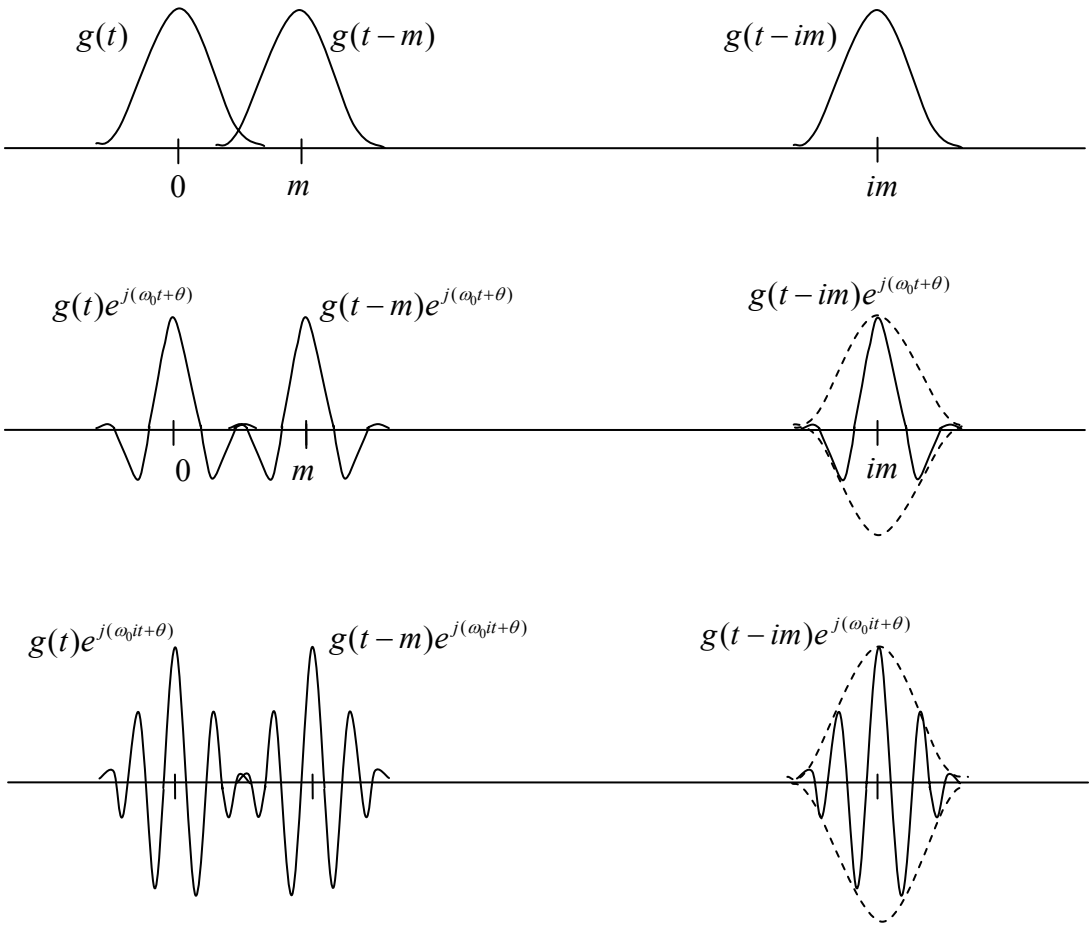

Figure 3.3 Gabor's elementary functions

In the above figure, $g_{i,m}(n) \equiv g_i(n-m)e^{j(\omega_0 in+\theta)}$ are the shifted and modulated copies of a single building block *g*. Each $g_{i,m}$ has an envelope of the shape of *g* (only the real part of the functions $g_{i,m}$ is shown).

Through empirical observations [34], we may model the short-time window function $g_i(n)$ as

$$g_i(n) = g(k:n) = \begin{cases} \exp\left(-\dfrac{n^2}{2k^2\sigma^2}\right), & |n| \le 2k\sigma \\ 0, & |n| > 2k\sigma \end{cases}, \forall i \tag{3.19}$$

where $\sigma \in R^+$ is the predetermined frame-size resolution, $(2k\sigma+1)$ is the frame size of $g(k:n)$ to be estimated and $k \in Z^+$. According to Eqs. (3.18) and (3.19), the elementary functions can be written as

$$g_{i,m}(n) = g(k:n-m)e^{j(\omega_0 n+\theta_i)}, \ \forall i,m \in Z^+. \tag{3.20}$$

Thus, according to the above equations (3.17) through (3.20) and Eq. (3.2), the noise-free ultrasonic signal *x(n)* can be approximated as

$$x(n) \approx \hat{x}(n) = \sum_i c_i g(k:n-d_i)\cos(\omega_0+\theta_i). \tag{3.21}$$

3.4 Determination of Signature Signal Parameters

As discussed in the previous section 3.3, the extracted signature signal, $\hat{\psi}(n)$ from Eq. (3.15) can be characterized by a parameter set $\{\omega_0, k, c_1, d_1, \theta_1\}$. $\hat{\psi}(n)$ is assumed to be a narrow-band signal. Thus, we can estimate its center frequency ω_0 as

$$\hat{\omega}_0 = \arg\max_\omega \left[|\Pi(\omega)|\right], \tag{3.22}$$

where $\Pi(\omega) = \sum_{n=-\infty}^{\infty} \hat{\psi}(n) e^{-j\omega n}$. The rest of parameters $\{k, c_1, d_1, \theta_1\}$ associated with it can be estimated as

$$\left\{\hat{k}, \hat{c}_1, \hat{d}_1, \hat{\theta}_1\right\} = \arg\max\left\{\rho\left[\hat{\psi}(n), c_1 g(k : n - d_1)\cos(\hat{\omega}_0 + \theta_1)\right]\right\}, \tag{3.23}$$

where $\rho\left[a(n), b(n)\right] \equiv \left| \dfrac{\sum_n a(n)b(n)}{\sqrt{\sum_n a^2(n)}\sqrt{\sum_n b^2(n)}} \right|$.

According to the Eqs.(3.22) and (3.23), the signature signal $\hat{\psi}(n)$ can be characterized as

$$\hat{\psi}(n) \approx \chi_1(n) = \hat{c}_1 g(\hat{k} : n - \hat{d}_1)\cos(\hat{\omega}_0 + \hat{\theta}_1). \tag{3.24}$$

3.5 Multiridge Detection Using Normalized Cross-correlation

Once we determine the parameters $\left\{\hat{\omega}_0, \hat{k}, \hat{c}_1, \hat{d}_1, \hat{\theta}_1\right\}$ associated with the approximated signature signal, $\chi_1(n)$, according to the Gabor analysis described in Sections (3.3) and (3.4), we can estimate the peak locations $\hat{n}_{\max,i}$, $i = 2,3,\cdots,L$, for the other ridges. Here both L and $\hat{n}_{\max,i}$, $i = 2,3,\cdots,L$, are unknown. Consider a *ridge resolution* parameter $\delta n_{\max}$ associated with the minimum spacing between any two adjacent ridges such that

$$\delta n_{\max} < n_{\max,i} - n_{\max,i-1}, \text{ for } i = 2,3,\cdots,L.$$

According to the aforementioned characteristics in Section 3.1 (mathematical model of ultrasonic signals), we can apply the *normalized cross-correlation function* $\gamma(m)$ between $x(n)$ and $\chi_1(n)$ to determine L and $\hat{n}_{\max,i}$, $i = 2,3,\cdots,L$, such that

$$\gamma(m) \equiv \frac{r_{x\chi_1}(-m)}{\sqrt{\sum_n \chi_1^2(n)}\sqrt{\sum_n x^2(n)}}, \quad m = 0,1,2,\cdots, \tag{3.25}$$

where $r_{x\chi_1}(-m) \equiv \sum_n x(n)\chi_1(n-m)$ is the cross-correlation function between the entire signal and the estimated signature.

After $\gamma(m)$ is obtained, the indices m should be sorted in an order $(m_1, m_2, m_3, \cdots)$ such that

$$|\gamma(m_l)| > |\gamma(m_{l+1})|, \text{ for } l = 1,2,3,\cdots. \tag{3.26}$$

If a *cross-correlation coefficient threshold* ς_{th} is chosen, then a set of indices m_l can be formed as $(m_1, m_2, \cdots, m_C)$ where

$$|\gamma(m_l)| < \varsigma_{th}, \text{ for } l = C+1, C+2, C+3, \cdots. \tag{3.27}$$

We would like to seek the subset B among the indices $(m_1, m_2, \cdots, m_C)$, which contains no adjacent ridges within the ridge resolution $\delta n_{\max}$. It can be defined as

$$B \equiv \left\{ l : |m_l - m_{l'}| > \delta n_{\max};\ l, l' = 1,2,\cdots,C;\ l \neq l' \right\}. \tag{3.28}$$

Thus the number of the ridges can be estimated as

$$\hat{L} = \#(B), \tag{3.29}$$

where $\#(B)$ is the number of the elements in the set B. Each peak location can be estimated as

$$\hat{n}_{\max,i} = \arg\max_{n \in \left[m_{B(i)} - \frac{\delta n_{\max}}{2} + 1,\ m_{B(i)} + \frac{\delta n_{\max}}{2} - 1 \right]} \{x(n)\}, \text{ for } i = 1,2,\cdots,\hat{L}, \tag{3.30}$$

where $B(i)$ is the i^{th} element in the set B.

3.6 Reconstruction of the signal

Once the ridges of the ultrasonic signal are obtained, the signal can be reconstructed according to Eq. (3.21) in Section 3.3 as

$$x(n) \approx \hat{x}(n) = \sum_{i=1}^{\hat{L}} c_i g(k : n - d_i) \cos(\omega_0 + \theta_i) . \tag{3.31}$$

3.7 Summarized Algorithm

Based on the analysis and the discussion in the previous sections, we propose a novel blind multiridge detection algorithm here. The complete procedure is provided as follows:

Step 1: *Initialization*

Set the threshold values: κ_{th}, ε_{th}, ς_{th} and $\delta n_{\max}$.

Step 2: *Optimal frame-size selection*:

Vary the frame-size N_f on the dyadic scale, $N_f = 2^1, 2^2, 2^3, \cdots$. For each N_f, compute $kur\left(E_{N_f,\Delta}(k)\right)$ according to Eqs. (3.4), (3.10), (3.11) and (3.12). Then determine the optimal frame size N_f^* according to Eq. (3.13).

Step 3: *Extraction of signature signal*

Set $N_f = N_f^*$. Then determine the parameters $\hat{p}_1, \hat{q}_1, \hat{n}_{\max,1}$ associated with the detected signature signal $\hat{\psi}(n)$ according to Eqs. (3.14), (3.15) and (3.16).

Step 4: *Modeling of signature signal parameters using Gabor Analysis*

Using the results from the step 3, the signature signal $\hat{\psi}(n)$ is mathematically modeled by the Gabor frames. Determine the parameters $\left\{\hat{\omega}_0, \hat{k}, \hat{c}_1, \hat{d}_1, \hat{\theta}_1\right\}$

according to the Eqs. (3.22) and (3.23). Then the signature signal can be modeled as $\chi_1(n)$ given in Eq. (3.24).

Step 5: *Construction of the normalized cross-correlation function*

Construct the normalized cross-correlation function $\gamma(m)$ between the entire signal $x(n)$ and the modeled signature signal $\chi_1(n)$ according to Eq. (3.25).

Step 6: *Determination of the number of ridges*

Form the sample index sequence $(m_1, m_2, \cdots, m_C)$ according to the *sort-and-select* procedure in Eqs. (3.26) and (3.27). Remove the *spurious ridges* within the ridge resolution and construct a set B of sample indices corresponding to the *true ridges* according to Eq. (3.28). The number of the ridges can be determined as $\hat{L}$ according to Eq. (3.29).

Step 7: *Detection of peak locations*

Finally, the peak locations $\hat{n}_{\max,i}$, $i = 1, 2, \cdots, \hat{L}$, can be obtained according to Eq. (3.30). Thus, the number of ridges, the begin and end of the ridges is obtained through these 6 steps. The next process is to obtain the reconstructed signal using the Gabor Transform.

Step 8: *Reconstruction of the Signal*

Using the modeled signature signal $\chi_1(n)$ obtained in step 4, the ridges of the original signal obtained from Steps 6 and 7, the whole signal can be reconstructed according to the Eq. (3.31).

3.8 Flow Chart

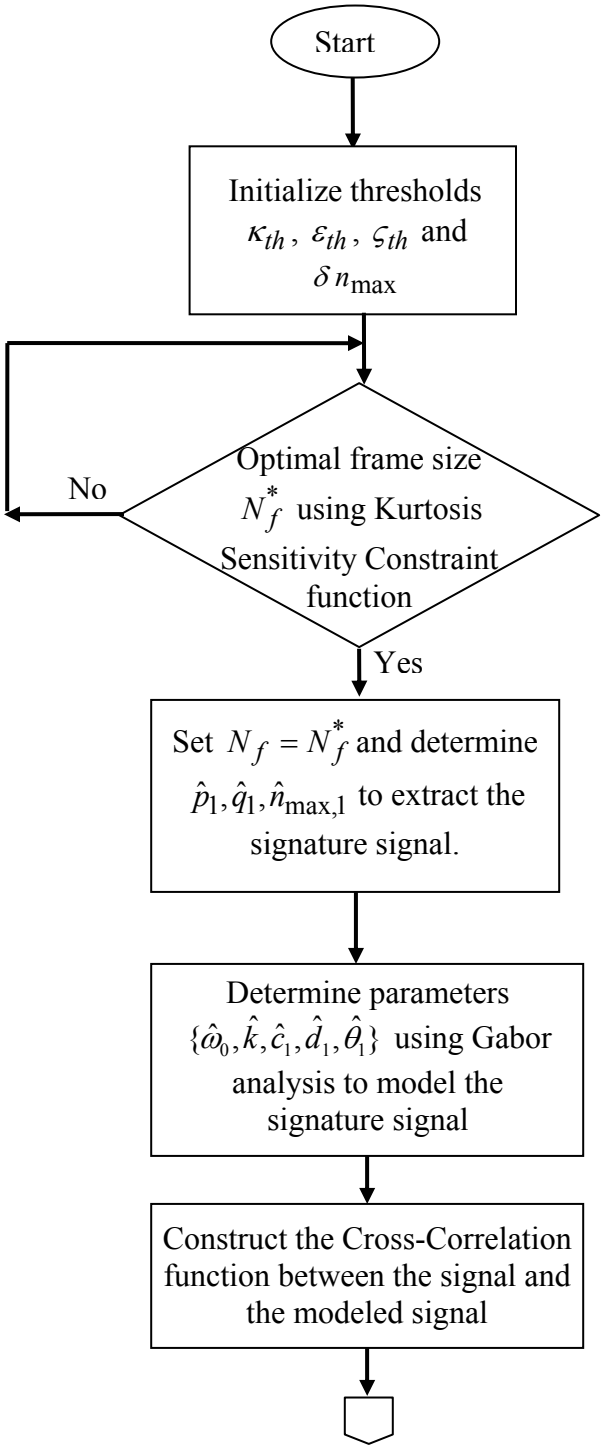

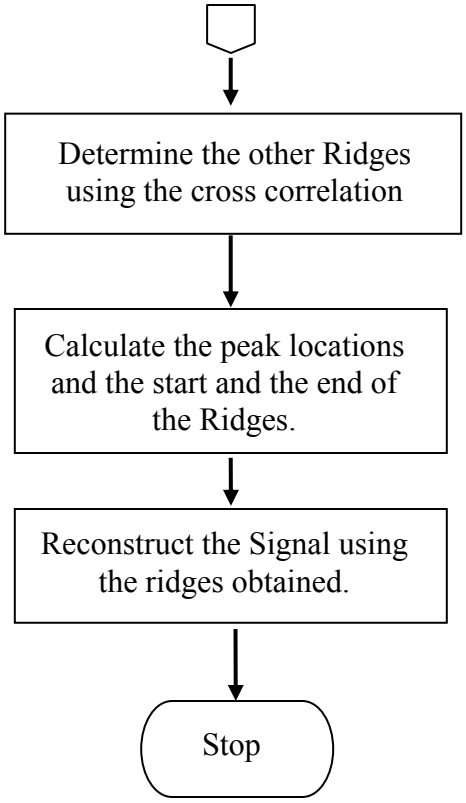

Figure 3.4 Flow chart of the Blind Multiridge Detection and Reconstruction algorithm for ultrasonic signals

Chapter 4: Simulation and Results

4.1 Acquiring the Ultrasonic Signals

In our work, the ultrasonic signals are acquired from the ultrasonic imaging equipment as illustrated in Figure (4.1). The ultrasonic imaging equipment was manufactured by Physical Acoustics Corporation.

Figure. 4.1 The ultrasonic imaging equipment.

The experiments are conducted on a set of different particle-filled composite specimens which are also called *particulate composites*. Specimens used in this study include composite materials filled with solid particles with a varying volume fraction from 0 to 50. The specimens are scanned by a pulse-echo transducer (the reflection method) at a frequency of 2.25 MHz [32]. These composite specimens can be very promising in structural aerospace applications because of their properties such as high strength to

weight ratio. As the percentage of the solid particles in the particulate composites change, the mechanical properties of the material such as structural strength also change. So, in this thesis, we detect the ridges and thereby try to detect the flaws (if any present) and also present a few applications of ridge detection in ultrasonic testing which help to study the mechanical behavior of the material.

4.2 Algorithm Implementation and Results

An ultrasonic signal waveform obtained from the ultrasonic imaging equipment for the particulate composite materials (with 10% volume of solid particles) is shown in Figure (4.2).

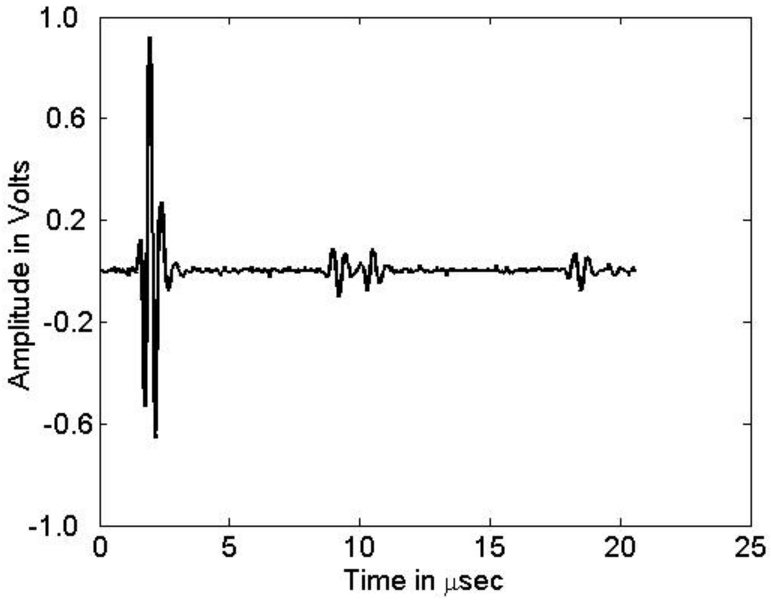

Figure 4.2 Ultrasonic signal waveform for composite material filled with 10%.volume of solid particles.

The above waveform shows two sets of front and back wall reflections obtained from the material sample where the first two peaks represent first set of front and back-wall reflections and the last two represent the second set.

The implementation of the algorithm is shown here for the composite material specimen filled with 10% volume of solid particles. E_1 is the energy for the first frame and E_{k_p} is the maximum framed energy. The threshold parameters are chosen as follows: $\kappa_{th} = 0.01$, $\varepsilon_{th} = 0.1E_{k_p} + 0.9E_1$, $\varsigma_{th} = 0.5$, $\delta n_{\max} = \frac{\hat{q}_1 - \hat{p}_1}{6}$. The next step in the algorithm is to obtain the optimal frame size.

4.2.1 Optimal Frame-size Selection

For signature signal extraction the optimal frame-size is the one for which the framed energy of the signal is smooth and compact in duration. The framed energy E_k for different frame-sizes ($N_f = 2, N_f = 16, N_f = 512$) is compared in Figures 4.3(a), 4.3(b) and 4.3(c), respectively.

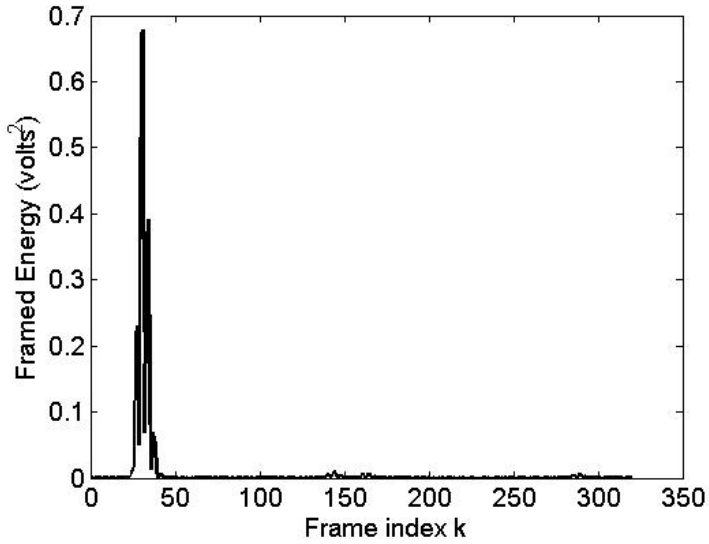

Figure 4.3(a). Framed energy sequence E_k with the frame-size $N_f = 2$.
(E_k is too spiky since the frame-size is too small.)

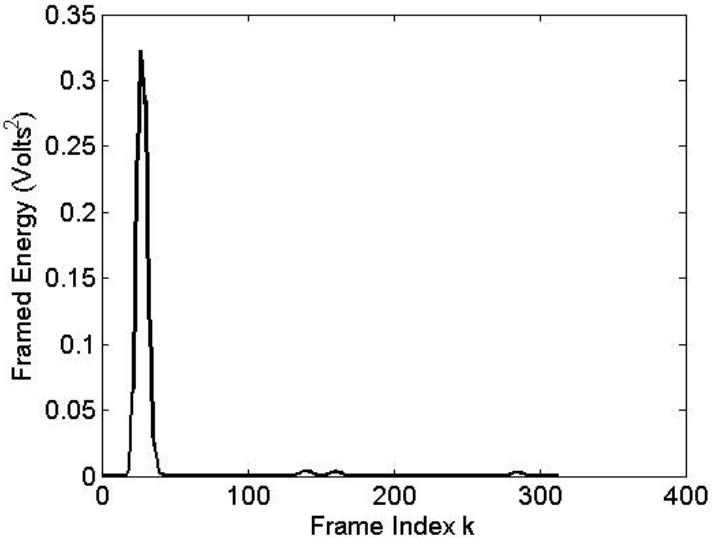

Figure 4.3(b). Framed energy sequence E_k with the frame-size $N_f = 16$.
(E_k appears to have a smooth and compact duration shape.)

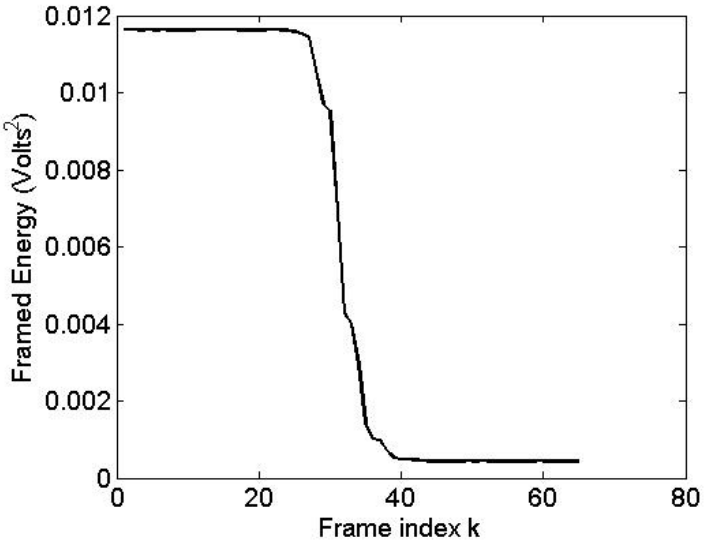

Figure 4.3(c). Framed energy sequence E_k with the frame-size $N_f = 512$.
(No ridge information can be perceived for detection since the frame-size is too large.)

As can be seen from the figures, a small frame-size $N_f = 2$ leads to a spiky-shaped E_k while a large frame-size $N_f = 512$ leads to an overtly smoothed E_k. Thus to obtain a smooth and compact duration E_k, as discussed in Section 3.2.3, the optimal frame-size

(for this particular case, i.e., for the specimen filled with 10% solid particles) is $N_f^* = 16$ and is as shown in Figure 4.3(b).

The optimal frame size for extracting the signature signal is data dependent and is obtained automatically from Step 2 of the algorithm using the threshold κ_{th}, the presumptive upper bound for the *kurtosis sensitivity constraint function*. The plot of the *kurtosis function* for the framed energy is shown in Figure (4.4).

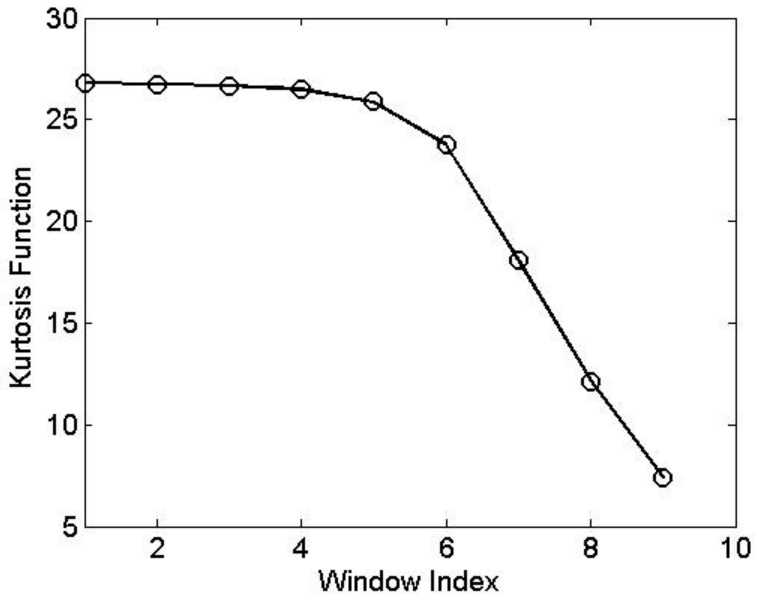

Figure 4.4 Kurtosis Function versus the frame size (2^0, 2^1, ..., 2^9) in terms of window index (0, 1,... 9)

The Kurtosis sensitivity function is obtained from Equation (3.13) in Section 3.2.3 which is nothing but the fractional change (Eq. 3.13) of the kurtosis function shown in Figure (4.4). The optimal frame-size is determined as the one for which the Kurtosis sensitivity function does not fall beyond the threshold κ_{th} and is 16 (2^4) in this case.

The effect of the frame-size N_f on the number of detected ridges can be shown in Figure (4.5), which is achieved when Step 2 is skipped and our multiridge detection procedures in Steps 1, 3, 4, 5, 6 are completed using the nine different defaulted frame-sizes. According to Figure (4.5), when the defaulted frame-sizes are $N_f = 2^1, 2^2$, many false alarms occur. On the other hand, when the defaulted frame-size is $N_f = 2^9$, a couple of ridges are not detected.

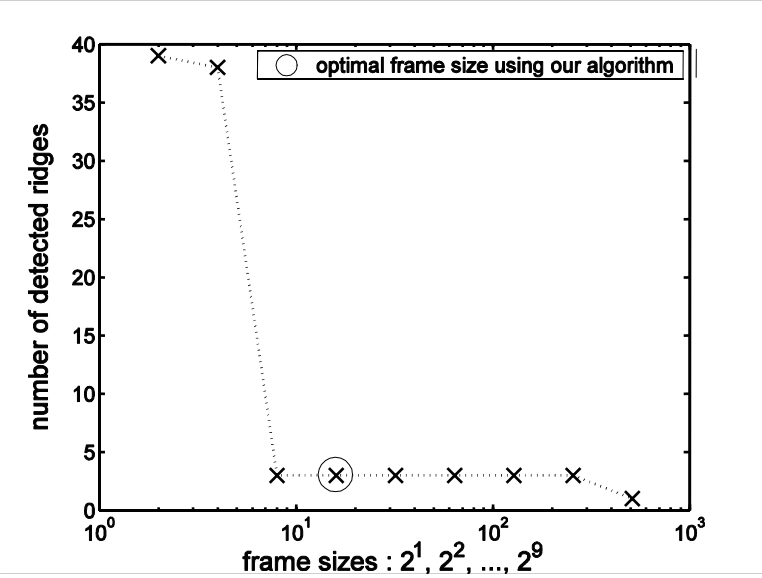

Figure 4.5 The number of detected ridges, $\hat{L}$, versus the frame size N_f where the true ridge number is *L*=3 and the optimal frame-size using our algorithm is $N_f^* = 16$.

According to Figure (4.5), the optimal frame-size should lie between 2^3 and 2^8 for the correct detection of ridges and hence, the optimal frame size achieved by our method $N_f^* = 16$ is reliable.

4.2.2 Signature Signal Extraction

Once the optimal frame size is obtained, the signature signal is extracted as mentioned in Step 3. The extracted signature signal $\hat{\psi}(n)$ is depicted in Figure (4.6).

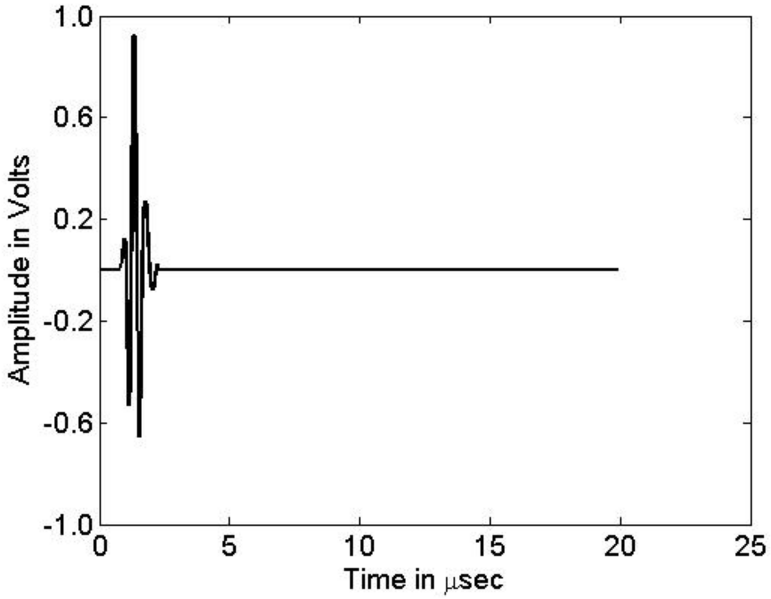

Figure 4.6 The signature signal $\hat{\psi}(n)$.

The absolute error graph is plotted by calculating the absolute error between the signature signal duration values obtained from the algorithm for each frame size and the observed values i.e.,

Absolute Error = |Calculated – Observed|

where Calculated = signature signal duration obtained from the algorithm

Observed = signature signal duration obtained manually.

The observed signature signal durations are obtained by manually marking the start and end of the signature signal and taking the difference between them.

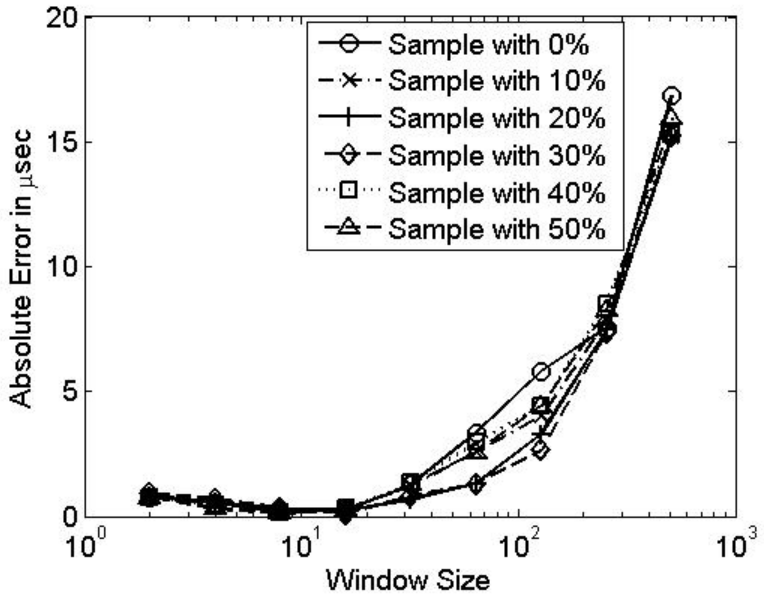

Figure 4.7 Absolute Error Graph

Figure (4.7) shows absolute error plots for six different particulate composite material specimens for which we conducted the experiments and tested our algorithm. This graph as shown in Figure (4.7) also presents that for the frame size $N_f^* = 16$ we have the least error and thus can be seen that it is the appropriate frame size for these specimens.

4.2.3 Signature Signal Modeling using Gabor Analysis

As mentioned in the section 3.3, the extracted signature signal is mathematically modeled using the Gabor frames. Using Step 4 of the summarized algorithm in section 3.7, the signature signal is characterized as the waveform shown in Figure (4.8).

4.2.4 Determination of Ridges

After obtaining the signature signal, the number of true ridges and their locations existing in the signal are obtained by following Steps 6 and 7 in the summarized algorithm. The peak location estimates $\{n_{\max,i}\}_{1 \le i \le \hat{L}}$ are shown in Figure (4.9).

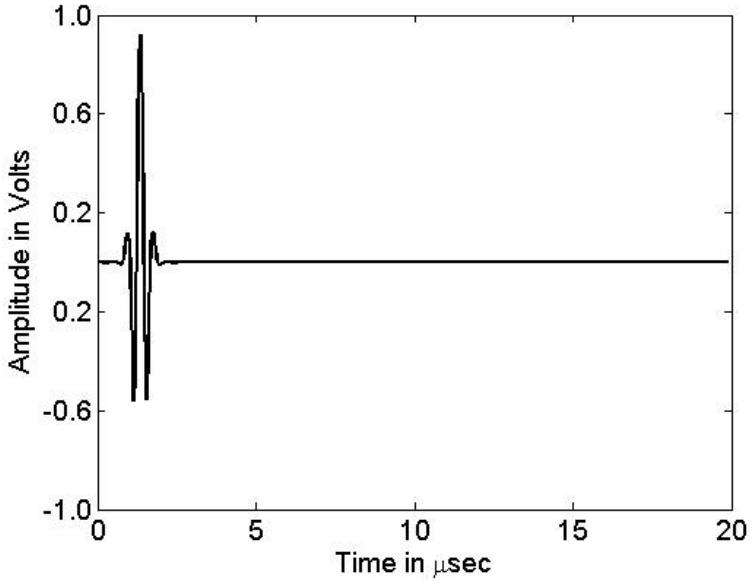

Figure 4.8 Simulated Signature Signal.

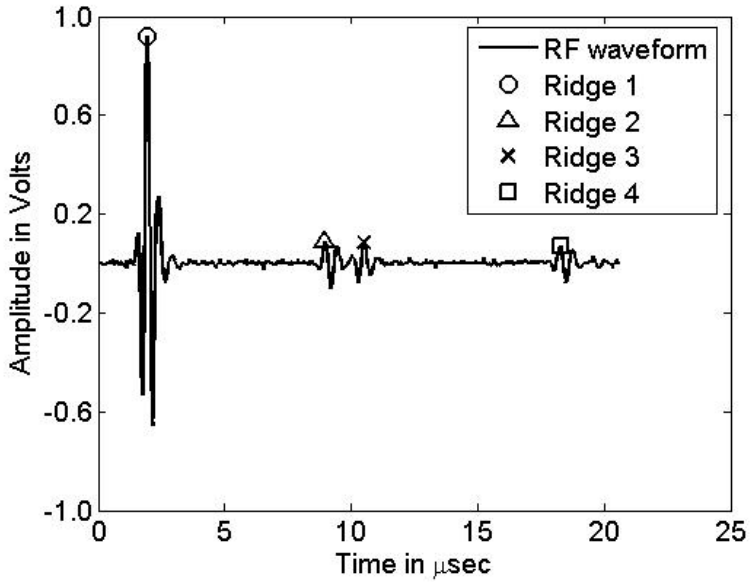

Figure 4.9 The detected ridges in an ultrasonic signal for composite material filled with 10%.volume of solid particles.

Figure (4.10) shows the peak locations for another material sample (with 30% particles filled). Our algorithm also detects a 5th peak in this material sample.

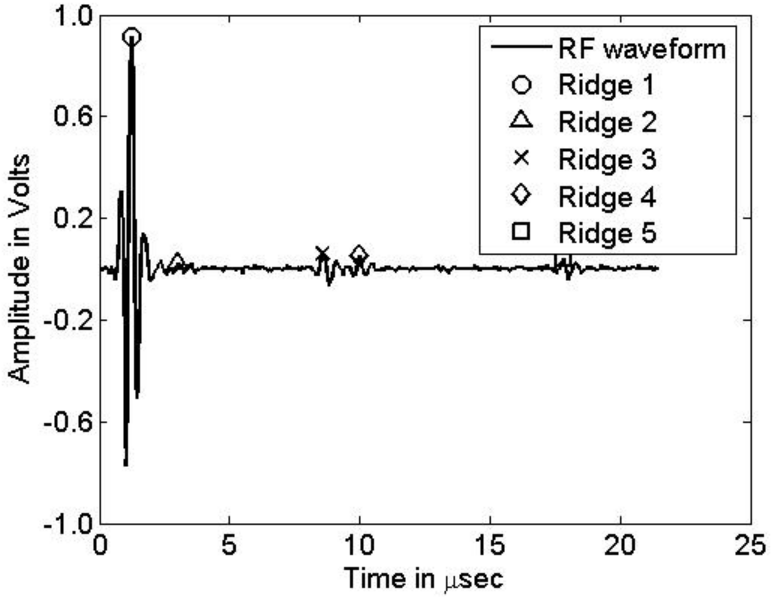

Figure 4.10 The detected ridges in an ultrasonic signal for composite material filled with 30% volume of solid particles.

Tables 4.1 and 4.2 show the peak amplitude values and the peak location values, respectively. The peak amplitude values for each sample in Table 4.1 have been normalized by their corresponding Peak 1 amplitudes. By observing the values in Table 4.1, it can be seen that as the percentage volume of the solid particles increases in the samples, the attenuation also increases.

Due to the attenuation of ultrasonic signal in the samples, the amplitude of back-wall reflection (peak 2) is lower than the front-wall reflection (peak 1). This amplitude further decreases as we go to the second set of backwall reflection (peak 4) thus showing that the samples cause attenuation. This attenuation for the sample with 50% solid

Table 4.1: The normalized ridge peak amplitudes for six solid particle filled samples

Samples with different % of solid particles	Peak 1	Peak 2	Peak 3	Peak 4
0%	1	0.14	0.13	0.10
10%	1	0.09	0.09	0.08
20%	1	0.05	0.05	0.04
30%	1	0.07	0.06	0.04
40%	1	0.06	0.06	0.03
50%	1	0.10	0.06	-

particles is so high that the second back-wall reflection (peak 4) is not even obtained in the signal. It is to be noted that all material samples were not of uniform thickness and hence the decrease in the amplitude values is not consistent. It can be seen from Table 4.1 that as the volume fraction increases, the intensity of the second back-wall reflection decreases. This can be attributed to the fact that as the number of particles in the particulate composites increases, the numerous reflections within the sample increase and thereby increases the attenuation of the ultrasonic signal. The decrease in the amplitudes with the increase in the percentage of solid particles can also be seen from Figure (4.2) and Figure (4.11) which show the waveforms obtained for the composite materials with 10% and 40% of solid particles respectively.

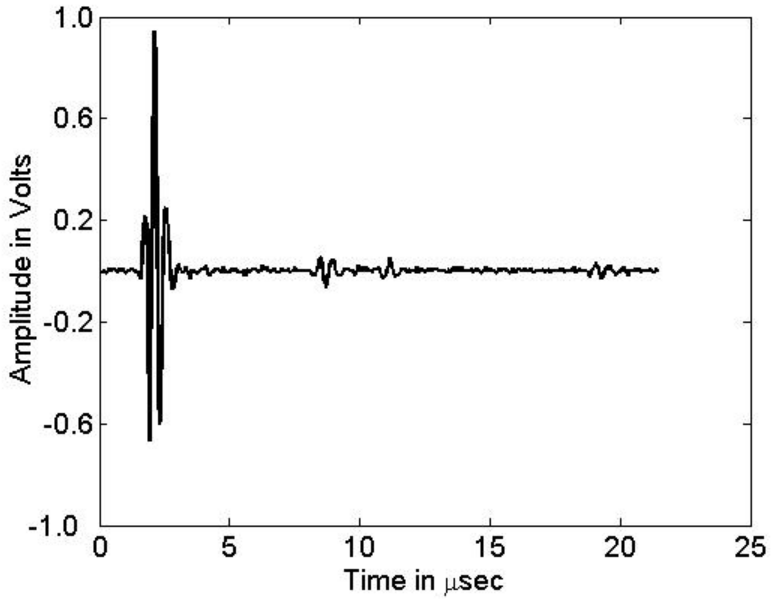

Figure 4.11 Ultrasonic signal for composite material with 40% solid particles.

As the distance between front and back-wall reflections are directly proportional to the thickness of the material, an estimate of the material thickness can be obtained from the Table 4.2.

Table 4.2: The ridge location information for six solid particle filled samples (in micro secs.)

Samples with different % of solid particles	Location of the Peaks in the signal (micro secs)				Distance bet. Peak 1 & 2
	Peak 1	Peak 2	Peak 3	Peak 4	
0%	3.49	10.78	11.94	19.81	7.30
10%	1.92	8.96	10.50	18.27	7.04
20%	1.06	7.52	9.57	17.31	6.46
30%	1.22	8.58	9.98	17.82	7.36
40%	2.11	8.51	11.17	19.04	6.40
50%	1.98	8.61	11.78	-	6.62

Table 4.2 shows the ridge location information for the front and back wall reflections alone. Hence, the second ridge for 30% sample as shown in Figure (4.10), which is possibly a defect or a misdetection, is ignored in this table.

In comparison, we also apply one other existing ridge detection technique for these material samples, and found that all ridges could not be detected using the Gabor transform in [11] no matter how we vary the frame sizes. The comparison between the two methods is illustrated in Figure (4.12). It shows the correct detection rate and false detection rate which are calculated based on the formula:

$$\textit{Correct Detection Rate \%} = (CR/TR)*100$$

$$\textit{False Detection Rate \%} = (FR/TR)*100$$

where TR = True number of ridges in the signal

CR = Number of ridges correctly detected

FR = Number of ridges falsely detected.

The number of falsely detected ridges includes both the false and misdetection of the ridges.

The plot shows that the maximum correct detection rate for a false detection rate of 20% is only about 50% using the method in [11], whereas for our technique it is around 90%.

4.2.5 Signal Reconstruction

The ultrasonic signal is reconstructed as in Step 8 and is shown in Figure (4.13). The original ultrasonic signal is shown in Figure (4.2) which very much resembles the reconstructed signal.

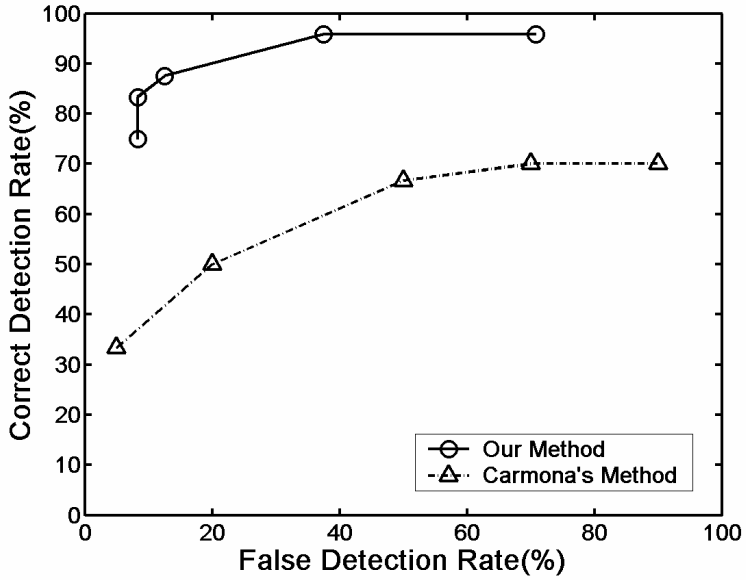

Figure 4.12 Comparison of Receiver Operating Curves (ROC) between our method and the method in [11]

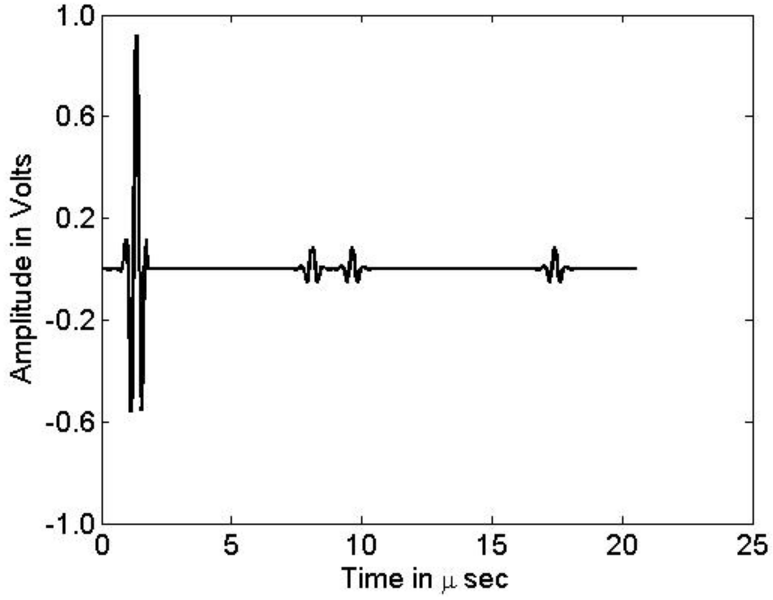

Figure 4.13 Reconstructed Signal

The Signal-to-Approximation-Error (SAE) between the original signal and the reconstructed signal is calculated and the values are tabulated in Table (4.3).

Table 4.3 The SAE of the ultrasonic signals in dB.

Samples with different % of solid particles	SAE in dB
0%	7.35
10%	11.32
20%	10.58
30%	9.90
40%	10.60
50%	8.82

4.3 Applications

In this section we present a few applications based on the ridge detection of our algorithm. The time difference between the front and the back wall ridges can be automatically calculated using the aforementioned algorithm. Consequently, the longitudinal velocities V_L of the ultrasonic waves in the particulate composites are calculated and compared for the six different material samples, as listed in Table 4.4. The longitudinal velocity V_L of the ultrasonic wave is calculated as the ratio between its traveling distance and time, i.e.,

$$V_L = \frac{D}{T},$$

where D and T are the wave traveling distance or twice the measured thickness of the specimen, and the time difference between the front and the back wall reflections, respectively. The manually calculated values are obtained by dividing twice the thickness

of the material with the manually marked distance between the front and back wall reflections.

TABLE 4.4 Comparison of ultrasonic wave velocities using manually marked and automatically computed time differences

Samples with different % of solid particles	Velocities V_L of Ultrasonic Waves in Composites, *m/s*	
	Manually marked	**Automatically computed**
0%	2717.30	2779.20
10%	2827.92	2866.50
20%	3296.02	3281.73
30%	2655.60	2690.21
40%	3184.70	3168.75
50%	3343.44	3324.28

In most cases the difference between the manually calculated and the automatically detected values is less than 2%. The manual operations of marking ridges in the ultrasonic signals are often susceptible to human errors and rather time consuming, especially in the presence of small-amplitude ridges as illustrated in figure (4.10).

The attenuation coefficient α of the material can be calculated using the amplitudes of the front and back wall reflections and is given by the equation:

$$\frac{A}{A_0} = e^{-\alpha x}$$

where A_0 and A are the front and back wall reflections respectively and x is the thickness of the material. The attenuation coefficient values obtained by manual calculation and by algorithm are listed in Table 4.5

TABLE 4.5 Comparison of ultrasonic wave attenuation coefficients

Samples with different % of solid particles	Attenuation Coefficient of the Composites	
	Automatically computed	**Manually calculated**
0%	0.19	0.19
10%	0.24	0.21
20%	0.29	0.26
30%	0.27	0.27
40%	0.28	0.26
50%	0.21	0.21

Other mechanical properties can be calculated using the following equations:

$$\textit{Poisson's ratio}:\ v = \left[1 - 2\left(\frac{V_S}{V_L}\right)^2\right] \Big/ \left[2 - 2\left(\frac{V_S}{V_L}\right)^2\right],$$

$$\textit{Shear modulus}: \text{(in GPa)},\ G = \rho V_S^2 \left(10^{-6}\right),$$

$$\textit{Bulk modulus}: \text{(in Gpa)},\ K = V_L^2 \rho - \frac{4}{3} G,$$

$$\textit{Young's modulus}: \text{(in Gpa)},\ E = \left(\rho V_L^2\right)(1 - 2v)(1 - v^2)\left(10^6\right)$$

where V_s, V_L and ρ are shear wave velocity, longitudinal wave velocity and specimen density respectively. Shear wave velocity can be obtained using a shear wave transducer. Unfortunately, our equipment does not provide this feature. Once V_s, V_L and ρ are known, all the mechanical properties mentioned above can be determined which in turn help in studying the mechanical behavior of the materials.

Our algorithm was also tested on an adhesively bonded sample. Adhesive bonding is the most suitable method for joining of both metallic and non-metallic structures where strength, stiffness and fatigue life must be maximized at a minimum weight [44]. The detected ridges for this sample can be seen in Figure (4.14).

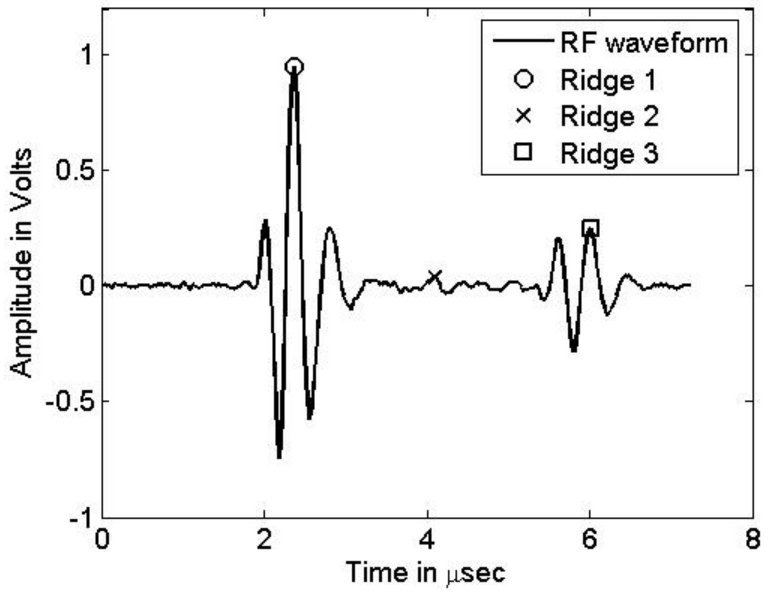

Figure 4.14 The detected ridges in an ultrasonic signal for a material with an adhesive joint.

In Figure (4.14) the ridge 1 and 3 represent the front and backwall reflections whereas the ridge 2 corresponds to the adhesive layer in the material sample. Due to the impedance mismatch between the CFRP (carbon fiber reinforced polymer composites) panels and the epoxy layer, an additional ridge (ridge 2) is observed which is detected by our algorithm.

Hence, our automatic blind multiridge detection algorithm would be promising to the efficient ultrasonic NDT applications in the future.

Chapter 5. Summary

In this thesis, we introduce a blind signal processing method for signature signal extraction, ridge detection and signal characterization using Gabor analysis without any need of *a priori* knowledge regarding the data statistics. The parameters in our blind detector are automatically adjusted for any given data and therefore no exhaustive offline model training is required in practice. Through numerous simulations, our proposed method provides the promising results when it is applied for ultrasonic signals in non-destructive testing. Some important mechanical properties such as Poisson's ratio, shear modulus and also the number of layers in the material sample can be automatically measured by a digital computer without any manual operation. Our method is crucial for the quality control of the material fabrication industry since the resulting signal characterization can lead to a wide variety of automatic mechanical property measurements in the near future. It can be foreseen that a novel computer tool can be generated using these blind signal processing techniques to automatically display the physical and mechanical measures, which will have broad impacts on the major industry in the future.

References

[1] N.Ozkurt, F.A. Savaci, "Evaluation of Instantaneous Frequencies by Singular Value Decomposition and Determination of the Degree of Chaoticity," *IJCI Proceedings of International Conference on Signal processing*, ISSN 1304-2386, vol. 1, no. 2, pp. 370-375, September 2003

[2] Online Dictionary – "http://www.hyperdictionary.com/dictionary/ridge"

[3] D. Guo, P. Richardson, "Automatic vessel extraction from angiogram images" *Computers in Cardiology 1998*, vol. 13-16, pp. 441-444, Sept.1998.

[4] B. Boashash, "Prolog to Estimating and Interpreting the Instantaneous Frequency of a Signal – Part 2: Algorithms and Applications", *Proceedings of the IEEE*, vol. 80, no. 4, April 1992.

[5] K. Grochenig, *Foundations of Time-Frequency Analysis* Birkhauser, Boston, 2001.

[6] N. Delprat, B. Escudie, P. Guillemain, R. Kronland-Martinet, P. Tchamitchian, B. Torresani, "Asymptotic Wavelet and Gabor Analysis: Extraction of Instantaneous Frequencies," *IEEE Trans. on Information Theory*, vol. 38, no. 12, pp. 644-664, March 1992.

[7] V. C. Chen, H. Ling, *Time Frequency Transforms for Radar Imaging and Signal Processing*, First Edition, Artech House Publishers, 2002.

[8] L. Cohen, *Time Frequency Analysis: Theory and Applications*, First Edition, Prentice Hall, 1994.

[9] S. Qian and D. Chen, *Introduction to Joint Time-Frequency Distribution Analysis – Methods and Applications*, Prentice Hall, Englewood Cliffs, NJ, 1996.

[10] M. I. Todorovska, "Estimation of Instantaneous Frequency of Signals using the Continuos Wavelet Transform", Technical report, Dept. of Civil Engineering, University of Southern California, Los Angeles, California, Dec 2001.

[11] R. A. Carmona, W. L. Hwang and B. Torresani, "Multiridge detection and time-frequency reconstruction," *IEEE Transactions on Signal Processing*, vol. 47, no. 2, pp. 480-492, February 1999.

[12] E. C. Johnson, J. D. Pollchik and J. N. Schurr, "An ultrasonic testing technique for measurement of the Poisson's ratio of thin adhesive layers," *Review of*

Progress in Quantitative Nondestructive Evaluation, eds. D. O. Thompson and D. E. Chimenti, vol. 11, pp. 1291-1298, Plenum Press, New York, 1992.

[13] G. G. Leisk and A. Saigal, "Digital computer algorithms to calculate ultrasonic wave speed," *Materials Evaluation*, pp. 840-843, July 1996.

[14] A. P. Mouritz, "Ultrasonic and interlaminar properties of highly porous composites," *Journal of Composite Materials*, vol. 34, no. 3, pp. 218-239, 2000.

[15] K. J. Newell, A. N. Sinclair, Y. Fan and C. Georgescu, "Ultrasonic determination of stiffness properties of an orthotropic viscoelastic material," *Research in Nondestructive Evaluation*, vol. 9, pp. 25-39, 1997.

[16] NDT Resource Center – "www.ndt.org"

[17] Nondestructive Testing", Louis Cartz Marquette university. Colege of Engineering, Milwaukee WI USA, ASM International

[18] W. Roye, "The reliability of nondestructive techniques within the field of modern composite materials," British Journal of Nondestructive Testing, vol. 33, no. 12, pp. 549-550, November 1991.

[19] NDT Resource Center "http://www.ndt-ed.org/EducationResources/Community College/Radiography/Introduction/history.htm"

[20] L. Mullins, "Evolution of NDT", *Progr. Appl. Mater. Res.*, vol. 5, E. G. Stanford, J. H. Fearson, and W. J. McGonnagle, Ed., 1964, pp. 205-212.

[21] *Ultrasonic Nondestructive Testing*, Monograph No. 9, The Institute of Metals, UK

[22] R. C. McMaster, *Nondestructive Testing Handbook: Liquid Penetrant Tests*, American Society for Nondestructive Testing, 1982.

[23] C. E. Betz, *Principles of Magnetic Particle Testing*, Magnaflux Corp, 1993.

[24] NDT Resource Center – http://www.ndt-ed.org/EducationResources/Comm unityCollege/MagParticle/Introduction/basicprinciples.htm.

[25] H. Krautkramer and J. Krautkramer, *Ultrasonic testing of materials*, Springer-Verlag, New York, 1969.

[26] J. Szilard, *Ultrasonic Testing*, John Wiley, 1982.

[27] *The NDT Yearbook*, British Institute of Nondestructive Testing, UK, 1987.

[28] R. J. Urich, *Principles of Underwater Sound*, McGraw-Hill, 1975.

[29] B. Carlin, *Ultrasonics*, McGraw-Hill, 1960.

[30] S. Sokolov, "Ultrasonic Methods for Determining Internal Flaws in Metal Objects", *Zavod. Lab.*, vol. 4, 1935, pp. 450-461.

[31] M. G. Silk, *Ultrasonic Transducers for NDT*, Adam Hilger, 1984.

[32] H G Tattersall, "The Ultrasonic Pulse-Echo Technique as Applied to Adhesion Testing," *J. Phys. D: Appl. Phys.*, vol. 6, pp.819-832, 1973.

[33] J. Krautkramer, H. Krautkramer., *Ultrasonic Testing of Materials*, Second Edition, Springer, Berlin, Heidelberg, and New York, 1977.

[34] A. M. Sabatini, "A Digital-Signal-Processing Technique for Ultrasonic Signal Modeling and Classification," *IEEE Transactions on Instrumentation and Measurement*, vol. 50, no. 1, pp. 15-21, February 2001.

[35] H. L. Van Trees, *Detection, Estimation and Modulation Theory*, Wiley, 2001.

[36] R. A. Carmona, W. L. Hwang and B. Torresani, "Characterization of Signals by the Ridges of their Wavelet Transforms," *IEEE Transactions on Signal Processing*, vol. 45, no. 10, pp. 2586-2590, October 1997.

[37] M. Frisch and H. Messer, "Detection of a Known Transient Signal of Unknown Scaling and Arrival Time," *IEEE Transactions on Signal Processing*, vol. 42, no. 7, pp. 1859-1863, July 1994.

[38] B. Woodward and H. Sari, "Digital Underwater Acoustic Voice Communications," *IEEE Journal of Oceanic Engineering*, vol. 21 , no. 2 , pp. 181-192, April 1996.

[39] Q. Li, J. Zheng, A. Tsai, Q. Zhou, "Robust Endpoint Detection and Energy Normalization for Real-Time Speech and Speaker Recognition," *IEEE Transactions on Speech and Audio Processing*, vol. 10 , no. 3, pp. 146-157, March 2002.

[40] H. C. Wu, N. Gupta and P. S. Mylavarapu, "Blind Multiridge Detection for Automatic Non-destructive Testing Using Ultrasonic Signals," 1st Revision, *IEEE Transactions on Signal Processing*, 2005

[41] J. G. Proakis and D. G. Manolakis, *Digital Signal Processing*, Third Edition, Prentice-Hall, New Jersey, 1996.

[42] A. M. Mood, F. A. Graybill and D. C. Boes, *Introduction to the Theory of Statistics*, Third Edition, McGraw-Hill, Boston, 1974.

[43] D. Gabor, “Theory of communication,” *Journal of IEE*, vol. 93, part III, no. 26, pp. 429-457, 1946.

[44] L. H. Lee, *Adhesive Bonding*, Plenum Publishing Corporation, New York, 1991.

Vita

Rekha Katragadda was born in 1981 in Andhra Pradesh, southern state of India. She graduated from high school in the year 1998. She finished her bachelor of engineering degree in electrical and communication engineering at Jawaharlal Nehru Technological University, India, in 2002. She is currently a candidate for the degree of Master of Science in Electrical and Computer Engineering at Louisiana State University.